Article

Odour motion sensing enhances navigation of complex plumes

https://doi.org/10.1038/s41586-022-05423-4

Received: 1 October 2021

Accepted: 6 October 2022

Published online: 9 November 2022

Check for updates

Nirag Kadakia[1,2,3], Mahmut Demir[1,2], Brenden T. Michaelis[4], Brian D. DeAngelis[1,2,5], Matthew A. Reidenbach[4], Damon A. Clark[1,2,5,6]✉ & Thierry Emonet[1,2,5,6]✉

Odour plumes in the wild are spatially complex and rapidly fluctuating structures carried by turbulent airflows[1–4]. To successfully navigate plumes in search of food and mates, insects must extract and integrate multiple features of the odour signal, including odour identity[5], intensity[6] and timing[6–12]. Effective navigation requires balancing these multiple streams of olfactory information and integrating them with other sensory inputs, including mechanosensory and visual cues[9,12,13]. Studies dating back a century have indicated that, of these many sensory inputs, the wind provides the main directional cue in turbulent plumes, leading to the longstanding model of insect odour navigation as odour-elicited upwind motion[6,8–12,14,15]. Here we show that *Drosophila melanogaster* shape their navigational decisions using an additional directional cue—the direction of motion of odours—which they detect using temporal correlations in the odour signal between their two antennae. Using a high-resolution virtual-reality paradigm to deliver spatiotemporally complex fictive odours to freely walking flies, we demonstrate that such odour-direction sensing involves algorithms analogous to those in visual-direction sensing[16]. Combining simulations, theory and experiments, we show that odour motion contains valuable directional information that is absent from the airflow alone, and that both *Drosophila* and virtual agents are aided by that information in navigating naturalistic plumes. The generality of our findings suggests that odour-direction sensing may exist throughout the animal kingdom and could improve olfactory robot navigation in uncertain environments.

Like many animals, insects sense odours using two spatially separated sensors—their antennae. This pair of sensors can detect local concentration differences, which encode odour concentration gradients and enable flies to navigate simple plumes such as steady ribbons, where gradients are resolvable and informative[17,18]. However, the relevance of bilateral sensing for natural plume navigation is less clear as, in turbulent flows, odour gradients fluctuate rapidly and do not reliably point towards the source[3].

Here we propose a distinct role for bilateral sensing: inferring the direction of motion of odour signals. To understand the 'motion' of an odour signal, picture smoke emanating from a chimney on a windy day. The dispersing smoke plume quickly breaks into disconnected filaments and, although these filaments move in seemingly random directions, their direction of motion at some instant is obvious by eye. We can think of the motion of odours (which are invisible) as analogous to the motion of these smoke filaments. Importantly, owing to the dispersive effects of turbulence and molecular diffusion, the direction of the filaments can differ from the wind[19], thereby providing a directional cue that is distinct from the local airflow.

To investigate whether flies sense and respond to odour motion, we first reanalysed a dataset of walking *Drosophila* navigating a complex, visualizable odour plume of which the odour statistics resemble those in turbulent flows[10] (Fig. 1a). In this plume, gradients can be randomly oriented relative to the source, and often differ substantially from the direction of odour motion (Fig. 1a (green and magenta vectors)). As the odour is visible, we can quantify the odour signal encountered during navigation, as well as infer the projections across the antennae of the odour gradient and of the odour velocity (which encodes the direction of odour motion) (Fig. 1b and Extended Data Fig. 1), while simultaneously measuring fly behaviour (Fig. 1b). Odour velocity was estimated by cross-correlating the odour concentration in the left and right antenna regions across subsequent frames (Methods), similar to methods that compute velocity using tracer particles in fluids.

Insects turn upwind when encountering odour signals[6,9,10,15], which we verified for flies oriented slightly away from the upwind direction (Fig. 1c (blue and red curves)). For flies already oriented upwind, there was no turning bias relative to the intensity or gradient of the odour (Fig. 1c,d). Notably, their turn bias did correlate significantly with odour velocity (Fig. 1e), suggesting that flies respond to the direction of odour motion in the absence of directional information from the wind.

[1]Department of Molecular, Cellular and Developmental Biology, Yale University, New Haven, CT, USA. [2]Quantitative Biology Institute, Yale University, New Haven, CT, USA. [3]Swartz Foundation for Theoretical Neuroscience, Yale University, New Haven, CT, USA. [4]Department of Environmental Sciences, University of Virginia, Charlottesville, VA, USA. [5]Interdepartmental Neuroscience Program, Yale University, New Haven, CT, USA. [6]Department of Physics, Yale University, New Haven, CT, USA. ✉e-mail: damon.clark@yale.edu; thierry.emonet@yale.edu

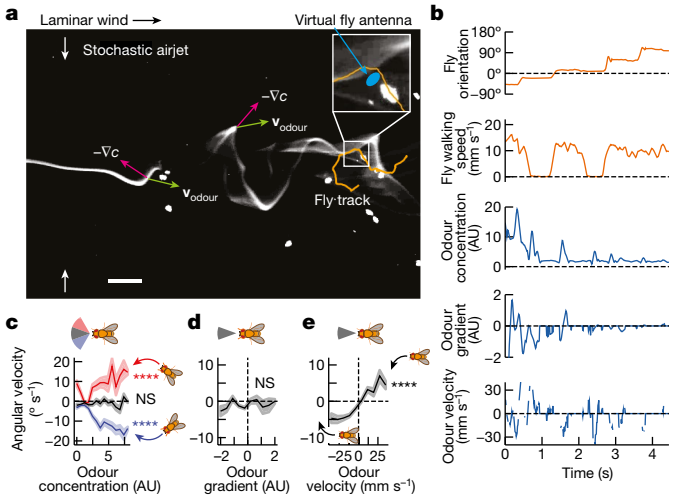

Fig. 1 | *Drosophila* turning behaviours are correlated with the direction of odour motion in a spatiotemporally complex odour plume. a, Snapshot of walking flies navigating a spatiotemporally complex odour plume generated by stochastically perturbing an odour ribbon in laminar flow with lateral airjets, as described previously[10]. Odour gradients (magenta arrows) and odour velocity (green arrows) do not necessarily align and can point in random directions relative to the odour source. The blue oval shows the virtual fly antenna region used to estimate signal quantities during navigation. Scale bar, 20 mm. **b**, Example time traces of fly behaviours (orange) and signal-derived quantities (blue) for the track shown in **a**. Odour velocity was computed by cross-correlating the signal in the virtual antenna over successive frames and determining the spatial shift with maximal correlation. Odour gradient was computed as the slope of the odour concentration along the major axis of the virtual antenna. AU, arbitrary units. **c**, Fly angular velocity as a function of odour concentration, for flies oriented in a 40° upwind sector (black), or in a 40° sector centred 40° clockwise (red) or counterclockwise (blue) from the upwind direction. Positive values indicate a counterclockwise turn. Data are mean ± s.e.m. Correlations are significant for flies in the off-axis sectors. Slope = 0.037 ± 0.005, n = 174 tracks; and slope = −0.039 ± 0.003, n = 312 tracks for clockwise and counterclockwise sectors, respectively. $P < 1 \times 10^{-6}$ for both sectors, but not those oriented directly upwind (slope = 0.005 ± 0.003, P = 0.09, n = 285 tracks). NS, not significant. **d**,**e**, Fly angular velocity versus odour gradient (**d**) and odour velocity (**e**) for flies oriented in a 40° sector upwind. Angular velocity is uncorrelated with odour gradient (mean slope = −0.005 ± 0.003, P = 0.072, n = 284 tracks) but significantly correlated with odour velocity (mean slope = 0.040 ± 0.003, $P < 1 \times 10^{-6}$, n = 282 tracks) across the virtual antenna. For **c**–**e**, statistical analysis was performed using two-tailed t-tests.

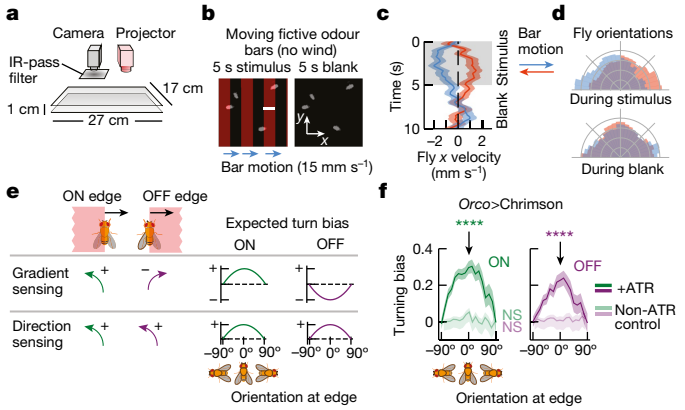

Fig. 2 | Turning responses are consistent with direction sensing, but not gradient sensing. a, Schematic of the optogenetic fly walking assay. Flies expressing Chrimson in ORNs received optical stimulation from a video projector mounted above the arena. IR, infrared. **b**, Fictive odour bars moving at 15 mm s^{-1} are presented in 5 s blocks, interleaved with a 5 s blank period. Scale bar, 5 mm. **c**, Component of fly walking velocity along the +x direction during the stimulus (shaded grey) and blank periods, for bars moving in the +x (blue; n = 178 tracks) or −x (orange, n = 192 tracks) direction. Data are mean ± s.e.m. Only flies facing in the 90° sector perpendicular to bar motion at odour onset (t = 0) are included. **d**, The distribution of fly orientations during stimulus (top) and blank (bottom) periods; colours are the same as in **c**. Orientations are symmetrized over the x axis. **e**, Direction sensing can be differentiated from gradient sensing by measuring turning responses versus fly orientation at both edges of wide, moving fictive odour bars: the ON edge (when the fictive odour first passes onto the fly) and the OFF edge (when it leaves the fly). **f**, Fly turning bias versus orientation for ON (green) and OFF (purple) edges moving at 10–15 mm s^{-1}. Darker curves indicate flies that were fed all-*trans* retinal (ATR); lighter curves indicate flies that were not fed ATR. Turning bias is quantified as the sign of orientation change after edge onset, where (+1) −1 is (counter) clockwise. Each point covers ±45°; thus, distinct points contain overlapping data. Data are mean ± s.e.m. Turning bias for ATR-fed flies, when oriented perpendicular to the bar motion (θ = 0), are significantly different from zero for both ON and OFF edges ($P < 1 \times 10^{-6}$ for both edges, χ^2 test; n = 1,673 and n = 1,509 ON and OFF edge encounters, respectively). Turning biases are not statistically distinct from zero for non-ATR fed flies (P = 0.09 and P = 0.77, χ^2 test; and n = 1,397 and n = 1,484 ON and OFF edge encounters, respectively).

Odour motion sensing without wind

Because odours are transported by the airflow, odour motion and wind motion are inherently connected. To break this connection, we turned to optogenetic stimulation of olfactory receptor neurons (ORNs) using the channelrhodopsin Chrimson[20,21]. We generated spatially complex, dynamic fictive odour stimuli using a DMD projector to display light patterns[22] onto blind, freely walking flies in the 27 × 17 cm^2 arena used in Fig. 1 (Fig. 2a). This set-up enabled optogenetic stimulation with sufficient spatial (<300 µm) and temporal (<6 ms) precision to hit fly antennae independently. We verified using electrophysiology and behavioural controls that optogenetic stimulation of Orco-expressing ORNs acts as an attractive fictive odour[21] (Methods and Extended Data Figs. 2a–c), and that flies walking either on the bottom glass or upside down on the top glass responded similarly to the signal (Extended Data Fig. 2d). Using this set-up, we first presented a simple stimulus consisting of travelling fictive odour bars in the absence of wind. Flies oriented perpendicular to the bar motion receive differential stimulation across their antennae when the edges of each bar pass across them. If flies responded selectively to the direction of fictive odour motion, we would expect opposing behaviours for bars travelling rightward versus leftward. We therefore presented 5-mm-wide bars travelling 15 mm s^{-1} either left or right, in 5-s-long blocks followed by a 5-s-long block of no stimulus (Fig. 2b). Indeed, right-moving bars elicited a net displacement of fly position to the left, and vice versa (Fig. 2c). Furthermore, flies oriented against the direction of motion during the 5 s stimulus block, but exhibited no asymmetry during the 5 s blank (Fig. 2d). Notably, both of these behaviours were absent in *Orco*>Chrimson flies with one antenna ablated (Extended Data Fig. 3a,b), but were preserved when Chrimson was expressed only in ORNs expressing the receptor Or42b (Extended Data Fig. 3c,d), which is known to drive olfactory attraction to vinegar[23] and represents a small fraction of all ORNs. These experiments suggested that the olfactory responses of the flies were direction selective, and that direction selectivity is enabled by bilateral sensing from the two antennae. The key indicator of direction selectivity was counterturning against bar motion—a reasonable response for locating an odour source emitting propagating odour signals.

Direction sensing at ON and OFF edges

As insects and vertebrates both detect spatial gradients of odour concentration and use them to navigate[18,24], we wondered whether gradient sensing could explain the directional biases that we observed.

We repeated the experiments described above with wider (30–45 mm) bars, which enabled us to quantify responses to each edge individually—the ON edge, when the fictive odour first passes over the fly, and the OFF edge, when fictive odour leaves the fly (Fig. 2e). Responses to these stimuli would clearly distinguish direction selectivity from gradient sensing, as gradient sensing would result in opposing behaviours at the ON and OFF edges, whereas direction-sensing responses would be the same (Fig. 2e). We calculated fly turning bias, defined as the sign of the cumulative change in orientation between 150 and 300 ms after the edge hit, as a function of the fly's orientation relative to the moving edge. For both ON and OFF edges moving at 10–15 mm s^{-1}, these plots had strong positive peaks for flies oriented parallel to the edge (that is, when the two antennae were stimulated differentially), indicating that the flies are responding to the odour motion, not the spatial gradient (Fig. 2f). Meanwhile, the responses were flat for control flies (Fig. 2f and Extended Data Fig. 3e). Repeating this for various bar speeds, we found strong directional selectivity for bars moving at 10 and 15 mm s^{-1}, whereas, for higher speeds (20–30 mm s^{-1}), the ON response was significant but reduced and the OFF response was abolished (Extended Data Fig. 3e). At slower speeds 1–5 mm s^{-1}, the ON response was still present, but the OFF response was now slightly negative, although not statistically significant (Extended Data Fig. 3e). We attributed this to gradient sensing in the slow edges, which are nearly static odour environments: odour direction and gradients are parallel for ON edges but antiparallel for OFF edges (Fig. 2e), so the behavioural responses to motion and gradients compound for the former but cancel for the latter. Finally, similar directional turning responses for both ON and OFF edges were present in *Or42b*>Chrimson flies (Extended Data Fig. 3f), indicating directional selectivity at the level of the single ORN type. These observations were robust to changes in the behavioural integration window (Extended Data Fig. 3g), consistent with previously reported reaction times for ON responses[9,25].

Odour motion sensing sums with wind sensing

Insects bias their heading upwind in the presence of attractive odours[6–8,10,12,15], but the role of odour motion in this upwind response is unknown. Our patterned optogenetic set-up enabled us to investigate this by independently controlling the wind and odour motion, which is otherwise prohibitive in natural environments. In our earlier experiments, we quantified turning bias in response to odour motion, but without wind (Fig. 2). In the presence of both wind and odour motion, we reasoned that fly responses would reflect some sort of summation of the responses to the isolated stimuli. We therefore presented fictive odours in the presence of wind, but without any motion of the odour. To remove odour motion, we flowed laminar wind and flashed the entire arena with light for 2.5 s, followed by 2.5 s of no stimulus (Fig. 3a). This stimulates both antennae simultaneously, removing bilateral information—an artificial stimulus that is difficult to deliver with natural odours. In this situation, flies bias their heading upwind (against the wind) at the onset of the flash (Fig. 3b), reminiscent of their tendency to turn 'against' the odour motion in the absence of wind (Fig. 2f and reproduced in Fig. 3c). The similarity of turning responses to wind and odour motion separately is illustrated by fitting the turning bias versus orientation plots to a sinusoid (Fig. 3b,c (dashed lines)). In both cases, the plots are well fit by $A\cos\theta$, where $A_{wind} = -0.40$ and $A_{odour} = -0.30$.

These simple functional forms encouraged us to consider a simple hypothesis for how flies respond to fictive odour edges moving at a given angle relative to the wind. We hypothesized that the response to the combined signal is a sum of the bar motion and odour motion responses. This hypothesis predicts that, when the odour motion direction and wind direction are aligned, the peak response should increase in magnitude and remain centred at 0° and 180° (Fig. 3d (first row)). If odour and wind motion oppose each other, these peaks should nearly cancel (Fig. 3d (middle row)). Finally, in the interesting case of wind and odour velocity perpendicular to each other, the peaks should shift leftwards to ~145° and ~325° (Fig. 3d (bottom row)). To test these predictions, we presented fictive odour bars either parallel, antiparallel or perpendicular to 150 mm s^{-1} laminar wind. When the wind and odour were aligned, the turning bias at ON edges was nearly perfectly fit by the additive prediction (Fig. 3e). The antiparallel motion of bars and odours was also fit well—extrema remained at 0° and 180°, although the cancellation overshot slightly. Notably, the response to perpendicularly oriented wind and odour reproduced the shift of the response curve peak from ~180° to 145°, and nearly reproduced the shift of the minimum from ~360° to ~325°. These results suggest that odour-direction-selective responses integrate with directional information from the wind in a largely, but not entirely, additive manner. Moreover, universally observed upwind turning responses are more complex than naive mechanosensory reactions triggered by the presence of odour—they can be enhanced and even cancelled by directional information from the odour itself. Interestingly, responses to OFF edges in the presence of laminar wind were very weak, suggesting that there are other nonlinear interactions between the loss of odour and wind (Extended Data Fig. 4).

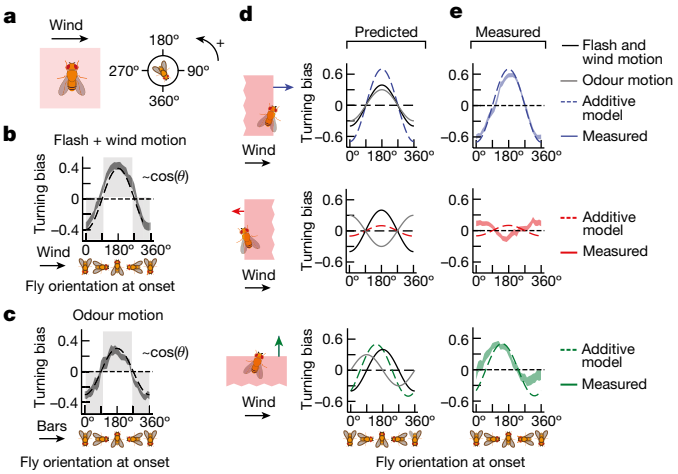

Fig. 3 | Turning responses to odour and wind direction are summed. **a**, Flashing the whole arena stimulates both antennae simultaneously, removing any directional odour cues. Laminar wind was introduced at 150 mm s^{-1}. **b**, Turning bias versus fly orientation, defined as in Fig. 2, for fictive bilateral odour flashes in the presence of wind (top; $n = 1{,}240$ odour hits). Data are mean ± s.e.m. Grey shaded boxed regions show the values for which the fly turns counter to the wind direction; all measured values lie in this range. The dotted line is fit to $-0.4\cos\theta$. **c**, Turning bias versus fly orientation for moving fictive odour bars without wind, at the ON edge (same data as the darker green curve in Fig. 2f, but without symmetrizing orientations). Grey shades indicate values for which flies turn counter to the bar direction. The dashed line is fit to $-0.3\cos\theta$. **d**, The expected turning bias versus orientation (dashed curve) for bars moving parallel (top row), antiparallel (middle row) or perpendicular (bottom row) to the wind, assuming that turning bias is the sum of the fitted cosines from **b** (black curve) and **c** (grey curve). In the middle and bottom row, the grey curve has a phase shift depending on the bar direction relative to the wind. **e**, The solid curves show the mean of measured data. Bars move at 15 mm s^{-1}. The dashed curves show the expected responses from **d**. The shaded regions show the s.e.m. $n = 1{,}361$, $n = 1{,}679$ and $n = 696$ ON edge hits for bars parallel, antiparallel and perpendicular to the wind, respectively. The additive model is also consistent with faster bar speeds, which have reduced responses (Extended Data Figs. 4e,f).

Odour motion sensing is correlation based

We next tested the extent to which our observations were consistent with elementary motion-detection algorithms. We began by analysing our data for moving bars in the absence of wind (Fig. 2).

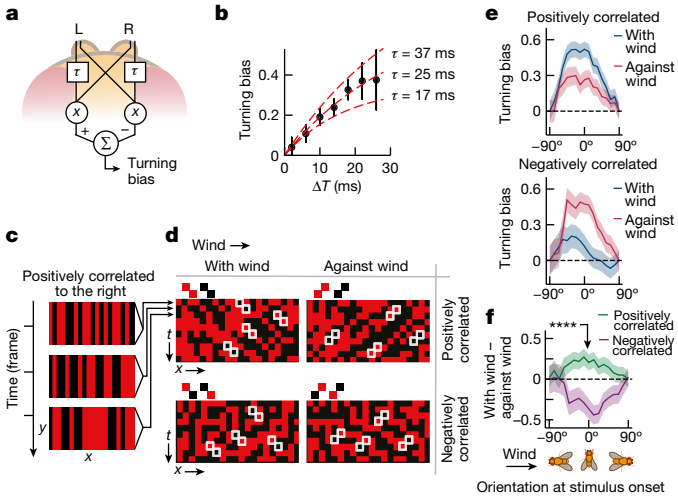

Fig. 4 | Odour motion sensing involves an algorithm that is sensitive to correlations. a, Schematic of a hypothesized HRC model in the olfactory circuit. **b**, The black dots show turning bias versus ΔT, using the moving bar data from Fig. 2f. Each datapoint spans ±4 ms. Middle (outer) red lines show the fit of the HRC model to the mean (±1 s.e.m.) of turning bias. $n = 1{,}475$ hits. **c**, Correlated noise stimuli consist of 1-pixel-wide fictive odour bars. In one frame (three frames are shown), each bar is independently light or dark. Here bars are positively correlated along $+x$, so a light bar at a given x in one frame is likely to be proceeded by a light bar one x-pixel to its right in the next frame. Visually, this appears as a rightward-moving pattern. **d**, Illustration of patterns over time for the four different types of correlated noise stimuli. Each pixel denotes the luminance of a bar at a given x position, at a given time. The four stimulus types are defined by correlation displacement (along $+x$, that is, with wind; or along $-x$, that is, against wind) and correlation parity (+ or −). For example, for with-wind positively correlated stimuli, bars are correlated with their right-side neighbours in the subsequent frame—this produces red–red or black–black diagonal patterns throughout the x–t plot. **e**, Turning bias versus fly orientation for positively correlated (top) and negatively correlated (bottom) stimuli. Stimuli are presented in 4 s blocks. Turning bias is defined as the sign of orientation change over 300 ms after stimulus onset. $n = 337$ and $n = 327$ onset events for with-wind and against-wind positively correlated stimuli; $n = 219$ and $n = 227$ for with-wind and against-wind negatively correlated stimuli. Data are mean ± s.e.m. **f**, The difference between the with-wind and against-wind responses from **e**, for positive (green) and negative (purple) correlations. Curves differed significantly for $\theta = 0$ ($P < 1 \times 10^{-6}$, χ^2 test).

Odour motion creates a difference in latency ΔT between the stimulation of the two spatially separated antennae, the sign and magnitude of which determines the output of direction-selective models such as the classical Hassenstein–Reichardt correlator (HRC)[16]. In our assay, ΔT can be inferred from the velocity of the bars relative to the flies using simple geometric considerations (Methods and Extended Data Fig. 5a). This enables us to express turning bias as a function of ΔT, thereby directly testing the predictions of an HRC model. In a simple rightward-selective HRC with two antennal inputs (Fig. 4a), a signal from the left antenna is multiplied with the delayed signal from the right antenna, where the delay is implemented as an exponential filter $e^{-t/\tau}$. Subtracting this product from a mirror-symmetric computation gives the detector output $r(t)$. We modelled the turning bias as the time integral of $r(t)$, for which the HRC predicts a turning bias proportional to $1 - e^{-\Delta T/\tau}$ for rightward-moving edges. Thus, plotting the turning bias against ΔT would enable us to extract the filter time constant τ for this model, revealing the timescale of olfactory motion detection. Pooling the data from both ON and OFF edges at 10–15 mm s^{-1} in the absence of wind (Fig. 2f), we found that the prediction was fit well, with filter timescales in the range $\tau = 25 \pm 12$ ms (Fig. 4b). Although this estimate is approximate and limited by the temporal and spatial resolution of the projector, it is notable that the timescale is comparable to those of visual motion detection in *Drosophila*[26] and humans[27].

Elementary motion detection algorithms respond fundamentally to correlations in the signal over space and time. To better compare behaviour to the predictions of the HRC, we moved beyond ON and OFF odour edges and turned to correlated noise stimuli, which have been used to characterize direction-selective computations in fly vision[26]. A snapshot of a correlated noise stimulus is a pattern of 1-pixel-wide bars, each of which is either light or dark (Fig. 4c). The pattern updates in time in such a way that it contains well-defined positive or negative correlations between adjacent pixels. Intuitively, a positive correlation in the $+x$ direction means that a light bar at a given x is likely—but not guaranteed—to be proceeded in the subsequent frame by a light bar 1 pixel to its right; visually, this would appear to be a rightward-moving pattern. To enhance the strength of the odour motion behaviour, we simultaneously flowed laminar wind as in the experiments in Fig. 3. Thus, there were four types of correlated noise stimuli, corresponding to the possible combinations of correlation displacement (with or against the wind) and parity (negative or positive) (Fig. 4d), each of which is uniquely defined by its correlation function $C(\Delta x, \Delta t)$ (Extended Data Fig. 5b).

In this experiment, turning responses to positively correlated noise stimuli mimicked those to moving bars: upwind turning was suppressed when the correlation displacement opposed the wind direction (Fig. 4e (top)). Importantly, spatial gradients in these stimuli quickly average to zero, so only a computation sensitive to spatiotemporal correlations, and not gradients, could account for behavioural suppression when the correlation displacement and wind were misaligned. Repeating for negative correlations, we found that upwind turning was suppressed when the correlation and wind were aligned (Fig. 4e (bottom)). Notably, this response is also consistent with a correlation-based algorithm, which predicts a reversal in the perceived direction of motion when the correlation changes sign[26]. In fact, this 'reverse phi' phenomenon is a common visual illusion—a feature of correlation-based algorithms—that has been observed and investigated across several species[26,28–30], including humans[31]. Subtracting the with-wind and against-wind responses for each polarity indicated clearly that the reverse-phi prediction was satisfied (Fig. 4f).

We corroborated our results using gliders, another class of correlated stimuli[32,33]. Visually, a glider is a random pattern of light and dark bars moving in one direction (Extended Data Fig. 5c). In contrast to correlated noise, the bars are correlated not only with a neighbouring bar in the subsequent frame, but also with more distant bars at later times. However, unlike the weaker magnitude correlations for correlated noise, the correlations in glider stimuli are perfect (Methods and Extended Data Fig. 5d), so we expected similar trends as before, but with larger effect sizes. For positively correlated gliders, we found similar trends as with correlated noise, but much larger separations between the with-wind and against-wind responses (Extended Data Fig. 5e). We were also able to examine a range of correlation times by adjusting the frame update times. For update times in the range of 17 to 30 ms, we found direction-selective responses, whereas, for shorter update times (11 ms), direction selectivity disappeared (Extended Data Fig. 5f). Interestingly, the maximum separation of with-wind and against-wind responses was with a frame update of 17–22 ms, consistent with the estimate of the HRC filter time constant using moving bars (Fig. 4b).

For flies to sense these correlations in our assay, their antennae must be optogenetically stimulated by distinct pixels. We satisfied this requirement by mounting the projector such that the x-pixel width (~290 μm) approximated the *D. melanogaster* antennal separation (Extended Data Fig. 5g). We predicted that effects would also reduce for bars wider than the antennal separation, as antennae were less likely to be stimulated independently. Indeed, when we repeated the experiments with the bar width doubled, we found no significant differences between with-wind and against-wind responses (Extended Data Fig. 5h).

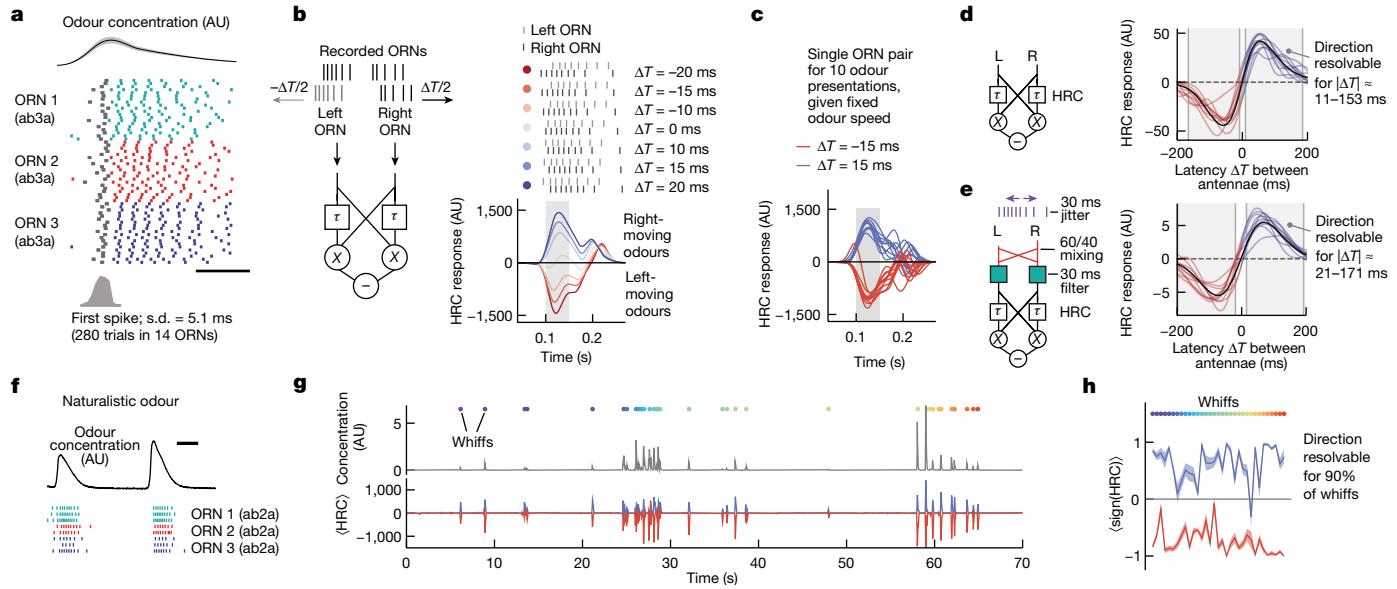

Fig. 5 | The temporal precision of ORN responses is sufficient to encode odour directionality. a, Spike rasters for ab3A ORNs responding to 50 ms puffs of ethyl acetate. Odours were presented 20 times each (rows) to different ORNs (colours) at 3 s intervals. The top trace shows odour concentration measured by PID. The histogram shows distribution of timing of first spike after odour presentation. Scale bar, 50 ms. **b**, HRC schematic (left). To calculate HRC responses to moving odour signals, ORN spike trains from **a** (taken from different ORNs in a single antenna) were designated as left or right antennal ORNs by adding appropriate delays. Right, HRC responses over time for various ΔT. **c**, The same as **b**, for the same pair of ORNs, over 10 different odour presentations and $|\Delta T| = 15$ ms. **d**, Time-averaged HRC response versus ΔT. The black line shows the mean over all pairings of left and right ORNs. The light curves show ten representative pairings. Odour direction is deemed to be resolvable if the mean is outside 1 s.d. of zero. As s.d. rather than s.e.m. is used, this corresponds to resolving odour direction with one odour presentation. **e**, The same as in **d**, but now including circuit transformations and noise. **f**, Representative ORN rasters to a few whiffs of a naturalistic odour signal (the full trace is shown in **g**). Scale bar, 100 ms. **g**, The odour signal (top) and the calculated mean HRC response ⟨HRC⟩ (bottom) for odour latencies of $\Delta T = \pm 15$ ms for a naturalistic odour signal. A total of 4 left and 4 right ORN spike trains were generated from 8 single antenna recordings as described in **b**, and the mean was taken over the 16 left–right pairs. The coloured dots show individual whiffs, defined by times at which the firing rate exceeded 30 Hz. **h**, The sign of the HRC response, averaged over 16 ORN pairs, for all whiffs in **g**. Data are mean ± s.e.m. over all 16 ORN pairs.

Together, these data suggest that *Drosophila* odour-direction sensing involves a correlation-sensitive algorithm.

ORN timing enables motion sensing

Our results so far have supported a correlation-sensitive model of direction sensing, tuned to interantennal odour latencies as short as ~15 ms (Extended Data Fig. 5f). This raises the question of how temporal precision in the olfactory periphery enables the detection of such latencies. To address this, we turned to electrophysiological measurements of odour-elicited ORN responses, using these to predict HRC model outputs for naturalistic stimuli. We recorded responses of 14 ab3A ORNs from one antenna in 2 flies to 20 short (50 ms) puffs of ethyl acetate (Fig. 5a). Across all 280 presentations, we found a jitter of 5.1 ms in the timing of the first odour-elicited spike, significantly smaller than in previous studies[34], but not insignificant compared with the 15 ms timescale of odour motion detection. To quantify how a correlator could extract directional information from noisy ORN responses, we chose at random a pair of spike trains measured in two different ORNs, shifted them in time by $-\Delta T/2$ and $\Delta T/2$, respectively, and we then passed this pair through the two arms of the HRC model (Fig. 5b). This procedure mimics how ORNs in each antenna would respond to a rightward-travelling odour filament, that is, the right ORN would receive the same signal as the left ORN, but ΔT later. Odour speed and direction are set by scaling or flipping the sign of ΔT, respectively. We found that for $|\Delta T|$ above around 10 ms, HRC output was positive for rightward-moving signals ($\Delta T > 0$) and negative for leftward-moving signals ($\Delta T < 0$; Fig. 5b), indicating directional selectivity. Moreover, HRC responses were very similar across odour presentation trials (Fig. 5c), meaning that odour direction could be extracted reliably without averaging over multiple encounters. Finally, extending this to all 19,600 possible pairings of 140 left and 140 right ORNs, we found that the simple HRC model could reliably resolve odour direction over a broad range of interantennal latencies $11 < |\Delta T| < 153$ ms (Fig. 5d), corresponding to odour speeds as high as 25 mm s^{-1}. Together, this indicated that, at least at the level of single, noisy ORN pairs, sufficient information was present to encode odour direction. Moreover, the HRC timescale of $\tau = 15$ms does not set a hard lower bound on the resolvable latency ΔT. This is because the filters in the HRC model smear the signals in time, so that HRC outputs are non-zero over a range of ΔT, not just when $\Delta T = \tau$. Thus, the HRC is strongly direction selective even at latencies far from τ.

Next, to see how some known downstream transformations might affect direction sensitivity, we added two processing steps upstream of the HRC computation: bilateral mixing of ORN signals with a 60/40 ratio[17] and a 30 ms low-pass filter representing projection neuron responses[34]. We also jittered each ORN spike up to 30 ms (ref. [34]) to represent variability across the ORN population. The aggregate effect of these three transformations was to shift the resolvable response range to $21 < |\Delta T| < 171$ ms (Fig. 5e)—a notably small reduction in sensitivity. In fact, we show mathematically that temporal filtering should not degrade the resolution to a level naively suggested by the filtering timescales. For example, an HRC receiving inputs that have been filtered over $\tau_{filt} = 100$ ms can still respond direction selectively to latencies much lower than τ_{filt} (Methods and Extended Data Fig. 6). Intuitively, while the projection neuron filter smears the two inputs, it acts on each input equally, thereby retaining the relative signal delay between them.

We next repeated the same calculations using the responses of ab2A ORNs to a naturalistic odour stimulus from our previous study[35], which is composed of brief bursts of odour, or whiffs, interspersed with periods of clean air (Fig. 5f). In this signal, the whiff concentrations

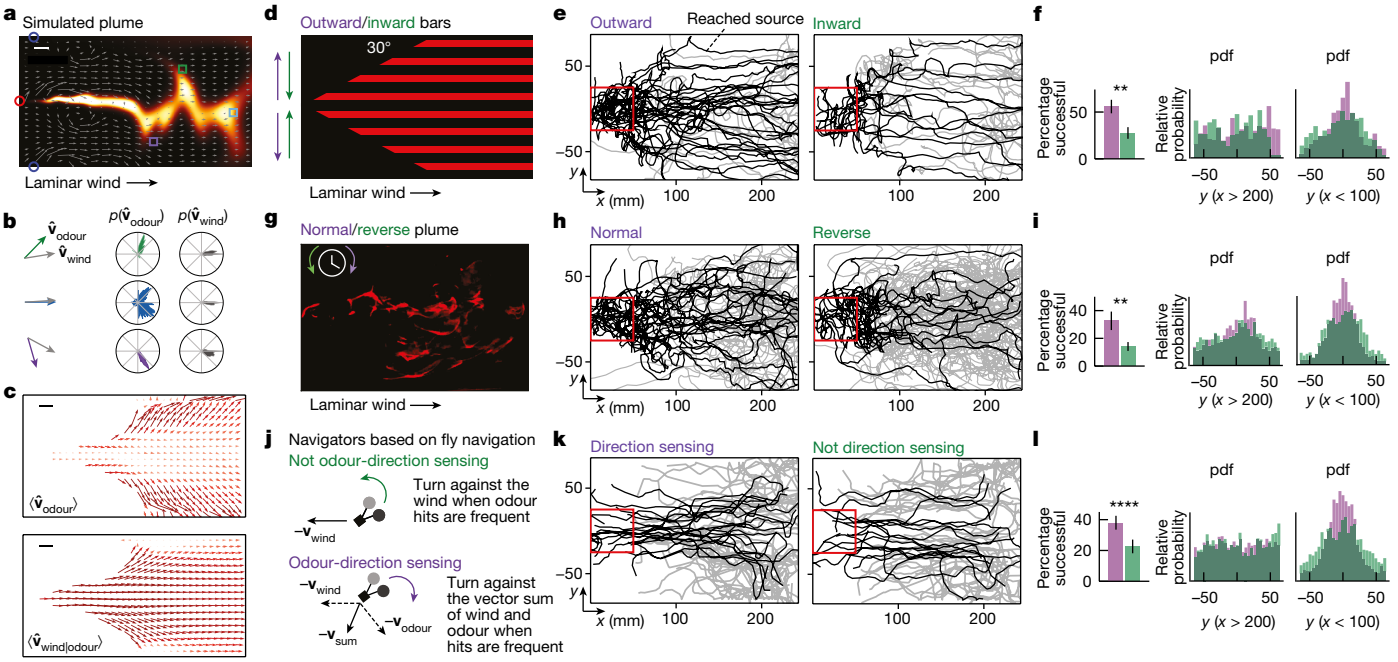

Fig. 6 | Odour-direction sensing enhances naturalistic plume navigation. **a**, Snapshot of the simulation of a plume from Fig. 1. The grey arrows show the wind direction at the instant of the snapshot. Scale bar, 20 mm. **b**, Odour (colours) and wind (grey) velocity vectors at the instant of the snapshot, at boxed locations in **a** (left). Middle and right, the distributions of the odour and wind velocity vectors over the whole simulation. **c**, The mean odour velocity field (top). Bottom, the mean wind field for detectable odour concentrations. Scale bars, 20 mm. **d**, Illustration of fictive odour plume in which 2-mm-wide bars move outwards or inwards from the arena centreline at 15 mm s^{-1}. Laminar wind flows at 150 mm s^{-1}. **e**, Measured fly tracks for flies beginning in the downwind 50 mm end of the arena, for outward (left) or inward (right) bars. The black tracks represent flies that reached a 50 mm box around the fictive plume source. **f**, Flies in the outward bar plume were more likely to reach the source (left): 56% (28 out of 50 tracks) versus 28% (12 out of 43 tracks) ($P = 1.13 \times 10^{-3}$, one-tailed *t*-test). Middle and right, the distributions of flies' lateral (*y*) position, in the downwind (left) or upwind (right) end of the arena, respectively. **g**, Projected complex plume, played either normally or in reverse. **h**,**i** Fly tracks (**h**) and quantification (**i**) as in **e** and **f** but for the complex plume in **g**. Flies in normal playback were more likely to reach the source: 32% (22 out of 69 tracks) versus 14% (13 out of 91 tracks) ($P = 6.39 \times 10^{-3}$, one-tailed *t*-test). **j**, Simulated agent model based on *Drosophila* odour navigation[10]. DS− agents increase the upwind bias of stochastic left/right turns with odour hit frequency (top; green). DS+ agents turn against the vector sum of the wind and odour directions as the hit frequency increases (bottom; purple). **k**, Tracks of DS+ (left) and DS− (right) agents navigating the complex plume in **g**. **l**, The same as **f** and **i**, but with DS+ and DS− agents. DS+ agents were more likely to reach the source (34% versus 25% of $n = 500$ tracks, $P = 9.98 \times 10^{-5}$; one-tailed *t*-test).

and durations spanned an order of magnitude, typical of odour statistics in turbulent flows[3]. We estimated the HRC response to left- and right-travelling odours as described above by pairing different recorded ab2A ORNs and shifting them appropriately (Fig. 5g). Averaging over all left and right pairs, we found that odour direction for latencies $|\Delta T| = \pm 15$ ms was resolvable in more than 90% of the individual whiff encounters (Fig. 5h). Together, these findings reveal that the temporal precision of ORN responses, together with putative circuit transformations in the *Drosophila* olfactory periphery, can robustly encode the direction of natural odour signals.

Finally, we note that, despite the robustness of the directionally selective odour computations shown above, our estimates here remain a worst-case scenario. We have simulated HRC responses using individual ORNs on each antenna, but *Drosophila* antenna contain populations of ORNs of each type, which are pooled in projection neuron responses. This convergence increases detection accuracy by averaging over noise[34,36], and a similar denoising upstream of direction sensing computations should enhance the robustness beyond what we have demonstrated here.

Odour motion sensing in natural plumes

In principle, animals could use measurements of odour motion to help them navigate complex plumes, provided this information complements other directional cues such as gradients or wind. To quantify the distribution of odour signal directions in a naturalistic plume, we ran numerical simulations of an environment replicating the plume from Fig. 1. These simulations provide not only a more finely resolved concentration field, but also the airflow velocity field (Fig. 6a), which is experimentally inaccessible. We first compared, for a few fixed points in the plume, the odour velocity $\mathbf{v}_{odour}$ and the airflow $\mathbf{v}_{wind}$ at a single time. Both $\mathbf{v}_{odour}$ and $\mathbf{v}_{wind}$ had *x*-components comparable to the mean flow speed 150 mm s^{-1}. However, $\mathbf{v}_{odour}$ also had large crosswind components $\mathbf{v}_{y,odour}$ pointing outwards from the plume centreline that were noticeably absent from $\mathbf{v}_{wind}$ (Fig. 6b (left)). Averaging over all detectable odour filaments in the 120 s simulation revealed a similar trend: away from the plume centreline, the distribution of $\mathbf{v}_{odour}$ spanned a tight angular range, pointing consistently outwards in the crosswind direction (Fig. 6b (middle column)). Meanwhile, $\mathbf{v}_{wind}$ was distributed largely downwind, with much smaller outward angles (Fig. 6b; right column). To visualize the flow of odour motion, we calculated the time average of $\langle \mathbf{v}_{odour} \rangle$ at all locations in the plume. We compared this to the time average of the wind vector conditional on the presence of odour, $\langle \mathbf{v}_{wind|odour} \rangle$. We used the latter rather than the unconditional wind velocity $\langle \mathbf{v}_{wind} \rangle$ because, for an ideal point source of odour within homogeneous turbulence, the latter does not encode the lateral location of the source. Throughout the plume, $\langle \mathbf{v}_{odour} \rangle$ flowed strongly outwards from the plume centre, whereas $\langle \mathbf{v}_{wind|odour} \rangle$ was directed essentially downwind (Fig. 6c).

This analysis suggests that, in naturalistic plumes emanating from a point source, the direction of odour motion is a strong indicator of the direction towards the centreline of the plume. This directional cue is

not reflected in the local wind, nor in the local gradients, although we did find that odour gradients have a similar crosswind structure closer to the source, where the plume is less intermittent (Extended Data Fig. 7a). Of course, to be useful for navigation, odour motion must be resolvable on realistic timescales. By calculating the running average of the odour direction at a fixed location, we found that in most of the plume extent, only several hundred milliseconds were necessary to resolve the lateral components (Extended Data Fig. 7b,c). As odour bursts occurred at around 1–5 Hz in this particular plume[10], a navigator could estimate the direction of odour motion orthogonal to the mean flow after only a few odour hits.

To investigate how *Drosophila* use odour motion during navigation, we designed a fictive odour plume of which the boundaries were subtended by a cone—as if emanating from a source—and within which thin bars moved laterally outward from or inward towards the centreline, while laminar wind flowed along the cone axis (Fig. 6d). The bars moved at 15 mm s^{-1} and were spaced by 5, 10 or 15 mm (data are pooled), giving fictive odour hits with short durations and frequencies of around 1–3 Hz, similar to the complex plume considered above (Fig. 1a). We reasoned that inward-moving bars, which are reversed from their natural flow, would degrade the ability of the fly to move towards the plume axis, and therefore to localize the odour source, that is, the tip of the cone. We found that, for both bar directions, flies stayed within the conical fictive odour region, but were significantly more likely to reach the upwind source region when the bars moved outwards (56% versus 28% for outward versus inward bars, respectively; $P < 0.01$, one-tailed *t*-test) (Fig. 6e,f). Moreover, performance gains were attributed to increased lateral navigation towards the plume centreline (Fig. 6f and Extended Data Fig. 8a), as predicted. Notably, the fictive odour signals in these two paradigms at each location do not differ by frequency, duration or spatial gradients—differences in performance (Fig. 6f) can be explained by odour-direction sensing alone.

Next, we tried the more realistic case of projecting a video of a recorded complex smoke plume, playing the video not only normally, but also reversed in time (Fig. 6g). As in the previous conical bar stimulus, reverse playback reverses odour motion without perturbing the steady-state distribution of spatial gradients or the frequency or duration of odour hits measured at each point. Notably, the likelihood to reach the odour source significantly degraded when the plume was played in reverse (32% versus 14%; $P < 0.01$, one-tailed *t*-test) (Fig. 6h), again driven by enhanced navigation towards the plume axis (Fig. 6i and Extended Data Fig. 8b). Together, these results indicate that the odour motion provides a directional cue complementary to odour gradients and wind motion, and strongly enhances navigation in complex odour plumes, even when other aspects of the odour signal remain unchanged.

Finally, with an eye towards practical applications, we used in silico experiments to investigate the value of odour motion sensing for olfactory robots. Virtual navigators were modelled as described in our previous study[10]: low-curvature walking bouts were interrupted with stochastic left/right turns at a fixed Poisson rate, and turns were more likely to be directed upwind as the frequency of odour hits increased (Fig. 6j). These virtual agents are not direction-sensing (DS− agents); meanwhile, direction sensing (DS+) agents obeyed the same strategy, but with turns biased against the vector sum of the odour motion direction and the wind direction (Fig. 6j). We simulated both DS+ and DS− agents in the imaged complex plume (Fig. 6g), finding that DS+ agents were better localized within the plume extent than DS− agents (Fig. 6k) and significantly more likely to find the odour source ($n = 500$ agents; 34% versus 25%, $P < 1 \times 10^{-4}$, one-tailed *t*-test) (Fig. 6l). As above, performance was aided by increased drift towards the plume centreline (Fig. 6l). These results were not a by-product of the model's behavioural repertoire—we found similar performance gains for direction-sensing virtual robots navigating a grid with a much simpler strategy (Extended Data Fig. 9). Together, these in silico experiments show that odour motion sensing can enhance the robustness of complex plume navigation in both simplistic and bioinspired navigational algorithms. The simplicity of the direction-sensing mechanism, together with computational methods to detect fast odour transients using metal oxide sensors[37,38], suggests that odour motion detection could be incorporated into olfactory robots in a variety of existing schemes[39,40] (see the Methods and Extended Data Fig. 10 for a discussion of the relationship between odour motion detection, the distance between the two sensors and the statistics of the turbulent air flow).

Discussion

Olfactory navigation relies on integrating various sensory signals that contain information about the odour source. Which features exist, and how much information they carry, can vary considerably between plume structures[41–43]. Gradient sensing can provide reliable directional information when navigating laboratory-controlled plumes, such as static ribbons[18], or very close to the source of natural plumes before odour patches have dispersed (Extended Data Fig. 7). However, further away from the source, turbulent air motion stretches and fragments odour patches as they are carried downstream, producing odour signals that are patchy and intermittent[1–3], and that span many spatial scales—the inertial convective range—from macroscopic eddies to molecular diffusion[44]. In these regions, concentration gradients tend to orient randomly, and therefore have limited value. Even in turbulent boundary layers, where concentrations are more regular[4], gradients could aid navigation, but would require amplifying the gradient to an extreme degree not consistent with data[6].

By contrast, our research suggests an entirely new role for bilateral sensing: measuring the direction of odour motion by comparing concentrations in both space and time. This information stream is especially relevant within the inertial convective range of turbulent plumes. Parallel to the plume axis, odour motion is redundant with the average wind direction. But perpendicular to the plume axis, odour packets spread through random continuous motions, with an effective diffusivity much larger than molecular diffusion[19]. What results is a strong flux of odour packets outward from the plume centreline, providing a directional cue orthogonal and, therefore, complementary to the mean wind. We corroborated this with a theoretical analysis of a simple turbulent plume model (Methods), finding that the outward flow of odour motion that we observed in simulations (Fig. 6c) exists in turbulent plumes more generally (Extended Data Fig. 10a,b). Moreover, these lateral odour velocity components can be detected by computing temporal correlations between two nearby points (Extended Data Fig. 10c). Thus, odour motion sensing is not just relevant to walking fruit flies—this directional cue could in principle enhance natural plume navigation across the animal kingdom, across distinct olfactory anatomies and in distinct locomotive regimes (Supplementary Text).

Our set-up enables us to test the predictions of the HRC model using artificial correlation-type stimuli which would be prohibitive to produce with natural odours. In particular, we generated a reverse-phi illusory percept for negative correlations, a signature of correlation-based algorithms observed in visual motion detection in flies[26,28] and other species[16,29,30], including humans[31]. Although the HRC model replicates several features of odour-direction sensing, it is an incomplete description of the odour motion sensing algorithm, neglecting asymmetries between ON/OFF responses and higher-order correlations in odour scenes (Supplementary Discussion).

Where direction selectivity occurs in the olfactory circuit is unknown. Most ORNs project to both antennal lobes, but ipsilateral and contralateral signals differ in magnitude and timing[17], which could be amplified further downstream to enact bilateral computations. One potential region of interest is the third-order olfactory centre, the lateral horn, which mediates innate odour responses and projects bilaterally[23,45].

The lack of smooth concentration fields in naturalistic plumes has inspired a number of navigation studies focusing on how animals use the temporal features of the odour signal, such as the frequency or duration of encounters with odourized air packets. This reliance on timing is enabled by the substantial degree of temporal precision in olfactory circuits[35,46–50]. Here we show that odour timing can be combined with bilateral sensing to measure odour motion, a directional cue that is distinct from the only other reliable directional cue in turbulent plumes—the wind. Our findings reveal a valuable role for bilateral sensing in the complex, dynamic odour environments that animals navigate in the wild.

Online content

Any methods, additional references, Nature Portfolio reporting summaries, source data, extended data, supplementary information, acknowledgements, peer review information; details of author contributions and competing interests; and statements of data and code availability are available at https://doi.org/10.1038/s41586-022-05423-4.

1. Murlis, J., Willis, M. A. & Cardé, R. T. Spatial and temporal structures of pheromone plumes in fields and forests. *Physiol. Entomol.* **25**, 211–222 (2000).
2. Riffell, J. A., Abrell, L. & Hildebrand, J. G. Physical processes and real-time chemical measurement of the insect olfactory environment. *J. Chem. Ecol.* **34**, 837–853 (2008).
3. Celani, A., Villermaux, E. & Vergassola, M. Odor landscapes in turbulent environments. *Phys. Rev. X* **4**, 041015 (2014).
4. Connor, E. G., McHugh, M. K. & Crimaldi, J. P. Quantification of airborne odor plumes using planar laser-induced fluorescence. *Exp. Fluids* **59**, 137 (2018).
5. Jung, S. H., Hueston, C. & Bhandawat, V. Odor-identity dependent motor programs underlie behavioral responses to odors. *eLife* **4**, e11092 (2015).
6. Alvarez-Salvado, E. et al. Elementary sensory-motor transformations underlying olfactory navigation in walking fruit-flies. *eLife* **7**, e37815 (2018).
7. Kanzaki, R., Sugi, N. & Shibuya, T. Self-generated zigzag turning of *Bombyx mori* males during pheromone-mediated upwind walking. *Zool. Sci.* **9**, 515–527 (1992).
8. Mafra-Neto, A. & Cardé, R. T. Fine-scale structure of pheromone plumes modulates upwind orientation of flying moths. *Nature* **369**, 142–144 (1994).
9. van Breugel, F. & Dickinson, M. H. Plume-tracking behavior of flying *Drosophila* emerges from a set of distinct sensory-motor reflexes. *Curr. Biol.* **24**, 274–286 (2014).
10. Demir, M., Kadakia, N., Anderson, H. D., Clark, D. A. & Emonet, T. Walking *Drosophila* navigate complex plumes using stochastic decisions biased by the timing of odor encounters. *eLife* **9**, e57524 (2020).
11. Vickers, N. J. & Baker, T. C. Reiterative responses to single strands of odor promote sustained upwind flight and odor source location by moths. *Proc. Natl Acad. Sci. USA* **91**, 5756–5760 (1994).
12. Budick, S. A. & Dickinson, M. H. Free-flight responses of *Drosophila melanogaster* to attractive odors. *J. Exp. Biol.* **209**, 3001–3017 (2006).
13. Suver, M. P. et al. Encoding of wind direction by central neurons in *Drosophila*. *Neuron* **102**, 828–842 (2019).
14. Flügge, C. Geruchliche raumorientierung von *Drosophila melanogaster*. *J. Comp. Physiol. A* **20**, 463–500 (1934).
15. Kennedy, J. S. & Marsh, D. Pheromone-regulated anemotaxis in flying moths. *Science* **184**, 999–1001 (1974).
16. Hassenstein, B. & Reichardt, W. Z. Systemtheoretische analyse der zeit-, reihenfolgen-und vorzeichenauswertung bei der bewegungsperzeption des rüsselkäfers chlorophanus. *Z. Naturforsch.* **11**, 513–524 (1956).
17. Gaudry, Q., Hong, E. J., Kain, J., de Bivort, B. L. & Wilson, R. I. Asymmetric neurotransmitter release enables rapid odour lateralization in *Drosophila*. *Nature* **493**, 424–428 (2013).
18. Duistermars, B. J., Chow, D. M. & Frye, M. A. Flies require bilateral sensory input to track odor gradients in flight. *Curr. Biol.* **19**, 1301–1307 (2009).
19. Taylor, G. I. Diffusion by continuous movements. *Proc. Lond. Math. Soc.* **20**, 196–212 (1922).
20. Klapoetke, N. C. et al. Independent optical excitation of distinct neural populations. *Nat. Methods* **11**, 338–346 (2014).
21. Bell, J. S. & Wilson, R. I. Behavior reveals selective summation and max pooling among olfactory processing channels. *Neuron* **91**, 425–438 (2016).
22. DeAngelis, B. D., Zavatone-Veth, J. A., Gonzalez-Suarez, A. D. & Clark, D. A. Spatiotemporally precise optogenetic activation of sensory neurons in freely walking *Drosophila*. *eLife* **9**, e54183 (2020).
23. Semmelhack, J. L. & Wang, J. W. Select *Drosophila* glomeruli mediate innate olfactory attraction and aversion. *Nature* **459**, 218–223 (2009).
24. Wu, Y., Chen, K., Ye, Y., Zhang, T. & Zhou, W. Humans navigate with stereo olfaction. *Proc. Natl Acad. Sci. USA* **117**, 16065–16071 (2020).
25. Bhandawat, V., Maimon, G., Dickinson, M. H. & Wilson, R. I. Olfactory modulation of flight in *Drosophila* is sensitive, selective and rapid. *J. Exp. Biol.* **213**, 3625–3635 (2010).
26. Salazar-Gatzimas, E. et al. Direct measurement of correlation responses in *Drosophila* elementary motion detectors reveals fast timescale tuning. *Neuron* **92**, 227–239 (2016).
27. Bours, R. J., Kroes, M. C. & Lankheet, M. J. Sensitivity for reverse-phi motion. *Vision Res.* **49**, 1–9 (2009).
28. Tuthill, J. C., Chiappe, M. E. & Reiser, M. B. Neural correlates of illusory motion perception in *Drosophila*. *Proc. Natl Acad. Sci. USA* **108**, 9685–9690 (2011).
29. Orger, M. B., Smear, M. C., Anstis, S. M. & Baier, H. Perception of Fourier and non-Fourier motion by larval zebrafish. *Nat. Neurosci.* **3**, 1128–1133 (2000).
30. Livingstone, M. S., Pack, C. C. & Born, R. T. Two-dimensional substructure of MT receptive fields. *Neuron* **30**, 781–793 (2001).
31. Anstis, S. M. & Rogers, B. J. Illusory reversal of visual depth and movement during changes of contrast. *Vision Res.* **15**, 957–961 (1975).
32. Hu, Q. & Victor, J. D. A set of high-order spatiotemporal stimuli that elicit motion and reverse-phi percepts. *J. Vis.* **10**, 9 (2010).
33. Clark, D. A. et al. Flies and humans share a motion estimation strategy that exploits natural scene statistics. *Nat. Neurosci.* **17**, 296–303 (2014).
34. Jeanne, J. M. & Wilson, R. I. Convergence, divergence, and reconvergence in a feedforward network improves neural speed and accuracy. *Neuron* **88**, 1014–1026 (2015).
35. Gorur-Shandilya, S., Demir, M., Long, J., Clark, D. A. & Emonet, T. Olfactory receptor neurons use gain control and complementary kinetics to encode intermittent odorant stimuli. *eLife* **6**, e27670 (2017).
36. Bhandawat, V., Olsen, S. R., Gouwens, N. W., Schlief, M. L. & Wilson, R. I. Sensory processing in the *Drosophila* antennal lobe increases reliability and separability of ensemble odor representations. *Nat. Neurosci.* **10**, 1474–1482 (2007).
37. Drix, D. & Schmuker, M. Resolving fast gas transients with metal oxide sensors. *ACS Sensors* **6**, 688–692 (2021).
38. Martinez, D., Burgues, J. & Marco, S. Fast Measurements with MOX Sensors: a least-squares approach to blind deconvolution. *Sensors* **19**, 4029 (2019).
39. Kowadlo, G. & Russell, R. A. Robot odor localization: a taxonomy and survey. *Int. J. Robot. Res.* **27**, 869–894 (2008).
40. Burgues, J., Hernandez, V., Lilienthal, A. J. & Marco, S. Smelling nano aerial vehicle for gas source localization and mapping. *Sensors* **19**, 478 (2019).
41. Boie, S. D. et al. Information-theoretic analysis of realistic odor plumes: What cues are useful for determining location? *PLoS Comput. Biol.* **14**, e1006275 (2018).
42. Jayaram, V., Kadakia, N. & Emonet, T. Sensing complementary temporal features of odor signals enhances navigation of diverse turbulent plumes. *eLife* **11**, e72415 (2022).
43. Reddy, G., Murthy, V. N. & Vergassola, M. Olfactory sensing and navigation in turbulent environments. *Annu. Rev. Conden. Matter Phys.* **13**, 191–213 (2022).
44. Sreenivasan, K. R. Turbulent mixing: a perspective. *Proc. Natl Acad. Sci. USA* **116**, 18175–18183 (2019).
45. Jefferis, G. S. et al. Comprehensive maps of *Drosophila* higher olfactory centers: spatially segregated fruit and pheromone representation. *Cell* **128**, 1187–1203 (2007).
46. Ackels, T. et al. Fast odour dynamics are encoded in the olfactory system and guide behaviour. *Nature* **593**, 558–563 (2021).
47. Martelli, C., Carlson, J. R. & Emonet, T. Intensity invariant dynamics and odor-specific latencies in olfactory receptor neuron response. *J. Neurosci.* **33**, 6285–6297 (2013).
48. Shusterman, R., Smear, M. C., Koulakov, A. A. & Rinberg, D. Precise olfactory responses tile the sniff cycle. *Nat. Neurosci.* **14**, 1039–1044 (2011).
49. Park, I. J. et al. Neurally encoding time for olfactory navigation. *PLoS Comput. Biol.* **12**, e1004682 (2016).
50. Nagel, K. I., Hong, E. J. & Wilson, R. I. Synaptic and circuit mechanisms promoting broadband transmission of olfactory stimulus dynamics. *Nat. Neurosci.* **18**, 56–65 (2015).

Methods

Fly strains and handling

Flies were reared at 25 °C and 50% humidity under a 12 h–12 h light–dark cycle in plastic vials containing 10 ml standard glucose-cornmeal medium (that is, 81.8% water, 0.6% agar, 5.3% cornmeal, 3.8% yeast, 7.6% glucose, 0.5% propionic acid, 0.1% methylparaben and 0.3% ethanol; medium was supplied by Archon Scientific). All flies used in behavioural experiments were female. Between 10 and 30 females were collected for starvation and placed in empty vials containing water-soaked cotton plugs at the bottom and top. All flies were 3–10 days old and 3 days starved when the experiments were performed. Flies in optogenetic experiments were fed 1 mM all trans-Retinal (ATR) (MilliporeSigma, previously Sigma-Aldrich) dissolved in water. ATR was fed to flies 1 day before recording, and all of the flies were housed in the dark from the time of ATR feeding until the time of the recording.

All of the flies used throughout the study included a *GMR-hid* transgene, which causes photoreceptors to die, making these flies blind. Optogenetic activation was achieved by expressing Chrimson (20X-UAS-CsChrimson) in *Orco*-expressing ORNs (Orco-GAL4) in almost all of the experiments[51]. The one exception was the single-Or experiments (Extended Data Fig. 3c,d), in which Chrimson was expressed only in neurons expressing the olfactory receptor Or42b.

The genotypes used were as follows: (1) *w;gmr-hid;+* (gift from M. Murthy); (2) *w;+;20XUAS-Chrimson* (Bloomington, 55136); (3) *w;+;Orco-Gal4* (gift from J. Carlson); (4) *w;+;Or42b-Gal4* (gift from J. Carlson); (5) *w;gmr-hid/+;20XUAS-Chrimson/Orco-Gal4* (Figs. 2–6, constructed from 1, 2 and 3); (6) *w;gmr-hid/+;20XUAS-Chrimson/Or42b-Gal4* (Extended Data Fig. 3c,d; constructed from 1, 2 and 4).

Behavioural assay and optogenetic stimulation

The fly walking arena is identical to the one used in a previous study[10]. All of the experiments were performed in a behavioural room held at 21–23 °C and 50% humidity. The walking arena is 270 × 170 × 10 mm (Fig. 2a) and consists of top and bottom glass surfaces and acrylic sidewalls. The upwind end is an array of plastic coffee straws, which laminarize the airflow (when wind is turned on); the downwind end is a plastic mesh. For experiments with wind, dry air was passed through the straws at a flow rate giving a laminar flow at 150 mm s^{-1} within the arena. The only exception was the forward and reverse playback complex virtual plumes (Fig. 6g), for which the laminar flow speed was reduced to 100 mm s^{-1} to match the flow speed used to generate the recorded smoke plume (see the 'Recorded smoke plume' section below). Flies were introduced by aspirating through a hole near the downwind plastic mesh. Flies were illuminated using 850 nm infrared LED strips (Waveform Lighting) placed parallel to the acrylic sidewalls.

Experiments were recorded at 60 Hz with a FLIR Grasshopper USB 3.0 camera with an infrared-pass filter. Optogenetic stimuli were delivered using a LightCrafter 4500 digital light projector (Texas Instruments) mounted 310 mm above the arena, illuminating an area larger than in the original method[22]. Only the red LED (central wavelength 627 nm) was used throughout this study. We used the native resolution of the projector (912 × 1,140 pixels), which illuminated the entire walking arena with pixels of size 292 µm (along the wind axis) × 146 µm (perpendicular to the wind axis). The majority of our experiments used a 60 Hz stimulus update rate; the exceptions were the faster 20–30 mm s^{-1} bar stimuli (Extended Data Figs. 3e and 4e,f), the glider experiments (Extended Data Figs. 5e,f) and the complex virtual plume playback (Fig. 6g), for which we used a 180 Hz update of projected images. The average intensity of the red light within the walking arena was 4.25 µW mm^{-2}. Although all data presented in this Article used blind flies, initial exploratory experiments used flies that were not blind. To remove visual effects from the stimulating red light, we shone green light using an LED (Luxeon Rebel LED 530 nm) throughout the arena to flood the visual response. Although this was not necessary for blind flies, we retained the green light throughout the experiments presented here to compare to past data.

The projector and camera have distinct coordinate axes—camera and projector pixels are different sizes and their native coordinate systems are not the same handedness. To infer the virtual encountered stimuli for navigating flies, one must transform between a 2D camera coordinate $\mathbf{x}_{cam}$ and a 2D stimulus coordinate $\mathbf{x}_{stim}$. We assume that the two are related by a combination of linear transformations and translations:

$$\mathbf{x}_{cam} = A\mathbf{x}_{stim} + \mathbf{B}.$$

To estimate the matrix A and vector $\mathbf{B}$, 3 mm diameter dots were projected at random locations $\mathbf{x}^i_{stim}$ in the arena while recording with the camera; camera coordinates $\mathbf{x}^i_{cam}$ were determined in the imaged frame using the SimpleBlobDetector function in OpenCV. The six elements of A and $\mathbf{B}$ were then determined by minimizing the least squares difference:

$$C = \sum_i (\mathbf{x}^i_{cam} - A\mathbf{x}^i_{stim} - \mathbf{B})^2$$

We verified manually that this procedure generated accurate transformations. We generated all stimuli using custom-written scripts in Python (v.3.7.4), and delivered these stimuli to the projector using the Python package PyschoPy (v.2020.2.4.post1).

Recorded smoke plume

The complex odour plume presented virtually with light (Fig. 6g) was derived from an imaged smoke plume in the same arena. The smoke plume was obtained using an identical protocol as in our previous work[10], but with slightly modified airflow conditions. There, the laminar flow speed was 150 mm s^{-1}, whereas here it was reduced to 100 mm s^{-1}. The speed of the two lateral perturbing upwind airjets was also reduced from ~1,500 mm s^{-1} to ~1,000 mm s^{-1}. The airjets were stochastically switched at a Poisson rate of 10 s^{-1} as in the original study. To convert the smoke plume to the virtual optogenetic plume, the images in the video were scaled with an affine transformation and presented with 8-bit resolution.

Electrophysiology

Single sensillum recordings from *Drosophila* antennae were performed as described previously[35,47,52]. The recording electrode was inserted into a sensillum on the antenna of an immobilized fly and a reference electrode was placed in the eye. Electrical signals were amplified using an Ext-02F extracellular amplifier (NPI electronic instruments). The ab2 sensillum was identified by (1) its size and location on the antenna and (2) test pulses of ethyl 3-hyrdoxybutyrate, to which the B neuron is very sensitive. Spikes from the A and B neurons in this sensillum were identified and sorted as described previously[35], using a spike-sorting software package written in MATLAB (MathWorks) (https://github.com/emonetlab/spikesort). For responses to real odour stimuli (Fig. 5), odours were delivered as in our previous work[35,53]. In brief, an odourized stream was fed into a main airstream and delivered through a glass tube positioned within 10 mm of the fly antenna, while mass flow controllers (Aalborg instruments and Controls, and Alicat Scientific) were used to regulate airflows.

Experimental protocol

Experiments were carried out between 09:00 and 12:00. This corresponds to between 0 and 3 h after lights on in our incubators, in which lights were on from 09:00 to 21:00. Between 10 and 30 flies were aspirated into the arena and allowed to acclimatize for 2 min before the experiments began. Before all of the experiments, optogenetic activation was verified by presenting static fictive odour ribbons (as in Extended Data Fig. 2c) with laminar wind for 120 s, and ensuring

that the flies followed the ribbons upwind as a positive control. In our assay, flies could walk on the top glass surface or bottom glass surface, and as the spacing between the surfaces was appreciable (1 cm), flies could flip to the top surface during a trial without climbing the sidewalls. In our videos, we could not reliably distinguish which surface the fly walked on, so we pooled flies for all analyses throughout. We verified that optogenetic activation of ORNs for flies on either surface was similar, by manually annotating 300 tracks of flies navigating fictive odour ribbons, and demonstrating that both similarly followed fictive odour ribbons upwind (Extended Data Fig. 2d). Unless otherwise noted, each experiment ran for 60–120 s, with 60 s in between the experiments.

No statistical tests were used to determine sample size. More than 50 flies were used for each experimental condition. As flies were reared in vials containing 10–15 individuals, this gave 5–10 vials per experimental condition, sufficient to mitigate outlier effects from any single vial. All of the experiments were replicated more than three times on the same flies, and the same conditions were replicated at least ten times with different flies over several days. Investigators were not blinded to fly genotype. Throughout, experiments were interleaved such that the directions of the moving stimuli were randomized. No more than 30 videos were recorded on a single set of flies.

Quantification of fly behaviour and encountered fictive odour stimulus

Extraction of fly position, speed and orientation from videos. All scripts were written in Python (v.3.7.4). Fly centroids were determined using SimpleBlobDetector in OpenCV, assuming a minimum area of 5 mm^2. Given the centroids, fly identities were determined using custom tracking scripts. In brief, centroids in subsequent frames were matched to the nearest centroid, and if the centroids could not be matched, they were marked as disappeared. Flies marked as disappeared for more than 30 frames (0.5 s) were then deregistered. Subsequent detected centroids were then marked as new fly tracks. Fly orientations θ were determined by first using the canny function in the Python module scikit-image to determine the points defining the fly edges around the centroid, then fitting these to an ellipse using custom-written Python scripts. Fly orientations are defined on the interval [0, 360°], but ellipse-fitting does not distinguish head (0°) from rear (180°). We properly resolved this using the fly velocity (below).

The above data defines the fly positions (x,y) and orientations θ. To remove measurement noise, we filtered each of these quantities with a Savitsky–Golay filter using a fourth-order polynomial and window size of 21 points (to avoid branch cuts in θ, it was first converted to an un-modded quantity). Velocities $\dot{x}$ and $\dot{y}$ and angular velocity $\dot{\theta}$ were defined by taking the analytical derivative of the fitted Savitsty–Golay polynomials for x, y, and θ. To resolve the two-fold symmetry in the fitted ellipses, and therefore distinguish the fly head from the rear, we used the fly velocity. For fly speeds greater than a given speed threshold, we matched the orientation to the fly velocity vector as flies predominantly walked forwards. For other times, we matched the fly heading at the beginning and end of bouts when the fly speed was below the speed threshold. The result was an estimate that may still have errors, which occur as unnatural jumps in orientation. We repeated this process for various speed thresholds from 1 to 4 mm s^{-1}, and chose the orientation trace with the least number of jumps. We verified manually with several tracks that this procedure was highly reliable.

We noticed that, during the experiments, particularly those with long fictive odour encounters such as the wide bars in Figs. 2 and 3, there was a slow, gradual bias towards one side of the arena (along the shorter axis of the arena). This occurred only for flies with optogenetic constructs that were fed ATR, and we reasoned that it might be due to a shadowing effect of the projector light from the fly body onto the antenna, or from one antenna onto the other, as the projector lens is nearer to the bottom of its projected image. This shadowing effect appears to create a fictive odour gradient across the arena. To account for this bias, we repeated all of the experiments that had an asymmetry in the perpendicular direction, such as bars perpendicular to the wind (Fig. 3d (third row)), in both directions. We then averaged the turning biases from these two directions, after flipping the orientations appropriately. This would retain the effects due to direction sensing but remove the bias, under the assumption that this bias was an additive effect.

Estimation of encountered fictive odour stimulus in antennae. Given these smoothed and corrected x, y, θ measurements, we then estimated the encountered fictive odour signal in the antenna region by defining a virtual antenna at a location 1.5 mm from its centroid along the ellipse major axis toward the fly head. To generate stable estimates—that is, not relying on a single pixel value—we use the stimulus value averaged over a box of 0.25 mm^2 around this location. Stimulus values in the antennal region are not measured by imaging, as the images are infrared-pass filtered. Rather, they are obtained from knowledge of the stimulus pattern and the stimulus-to-camera coordinate transformation defined above. In PsychoPy, stimulus values are defined as 8-bit integers, from 0 to 255, but in practice we deliver stimuli only as maximum intensity (255) or 0. Accordingly, we treat the signal in the virtual antenna as binary, equal to 1 when the average stimulus value in the 0.25 mm^2 region is above 200, and 0 otherwise.

Quantification of behaviour for moving bar stimuli. For all wide bar stimuli, only flies walking between 2 and 20 mm s^{-1} at the time of the edge hit were included. For fast-moving bars (Fig. 2b–d and Extended Data Fig. 3), only tracks lasting longer than 10 s and of which the mean speed was between 3 and 10 mm s^{-1} were included. For the bar stimuli in Figs. 2 and 3, we identified ON and OFF edge hits as the times that the antennal signal switched from 0 to 1 or 1 to 0, respectively, where this binarization was calculated as described above. To calculate turning biases, we followed previous work[10] and considered saccadic turning events, identified as points at which the absolute value of the angular velocity exceeded 100° s^{-1}, and ignored small jitters. Turn biases at a given time t_i (for example, at an ON or OFF edge hit (Figs. 2 and 3)) were defined as the sign of the change in fly orientation from t_i + 150 ms to t_i + 300 ms, provided that the absolute value of angular velocity in that window exceeded 100° s^{-1} at some point in that window. We used this 150 ms latency after t_i to account for uncertainties in t_i due to uncertainties in the exact position of the antenna, which we estimated as being upper bounded by 2 mm. For all plots, to remove tracks in which flies may have been turning before the hit, we ignored points for which the absolute angular velocity exceeded 100° s^{-1} between 300 ms and 150 ms before the hit. The dependence of the results on this window is shown in Extended Data Fig. 3g; although the effects are largest in this regime, they are not strongly sensitive to the choice of window following t_i.

Quantification of behaviour for correlated noise and glider stimuli. Turn biases for correlated noise and glider stimuli (Fig. 4) were calculated similarly to those for moving bars. Correlated noise and glider stimuli (Fig. 4) were presented in blocks of 4 s of stimulus interleaved with 4 s of no stimulus; thus, the stimulus turned on at times 0, 8, 16 s and so on. For correlated noise stimuli, we considered orientation changes from t_i to t_i + 300 ms, where t_i was time of the stimulus initiation (that is, 0 s, 8 s, 16 s and so on); the 150 ms latency used for bar stimuli was not needed in this case as the signal was independent of fly behaviour, so the hit time was known to the precision of the inverse frame rate (6 ms). For glider stimuli, we considered orientation changes from t_i + 200 ms to t_i + 500 ms stimuli as this gave the largest response. We also only included flies with speeds <12 mm s^{-1} for glider responses, as long-range correlations can interfere with the intended correlation if the fly walking speed is near the glider speed.

Plume simulations

Direct numerical simulations were generated using the CFX hydrodynamic simulation software package of Ansys 2019 (Ansys). Parameters were chosen to emulate the flow and intermittent odour structure of the plume analysed in Fig. 1 (ref. [10]). The mean flow speed was 150 mm s^{-1}, with an air viscosity of 1.5×10^{-5} m^2 s^{-1}. An odourant with molecular diffusivity $D_m = 7.3 \times 10^{-6}$ m^2 s^{-1} was injected mid-stream (vertically and horizontally). The odourant was modelled as a conservative, neutrally buoyant tracer. The dimensions of the computational model domain were 30 × 18 × 1 cm, approximately matching those of the walking arena[10]. The computational air inlet boundary was modelled as a uniform velocity condition, representing an idealized collimated flow. The outlet boundary condition was modelled as a zero-pressure gradient opening allowing for bidirectional flow across the boundary. Walls were modelled using hydraulically smooth, no-slip boundary conditions. To reproduce the stochastic airjets creating the complex flow and plume, alternating jet pulses of air were applied from two orifices on opposite sides of the flume. The time series of pulses were identical to the experiments[10]. The model domain was broken up into 4.7×10^6 tetrahedral elements where velocity and concentration were computed, with the largest element's length at 5 mm with an inflation layer along the domain boundaries and a refined mesh around the inlet orifices.

The flow was simulated at a 2.5 ms time step using a $k-\varepsilon$ eddy viscosity model[54], which solves the Reynold-averaged Navier Stokes equations, where the momentum equation is defined as:

$$\frac{\partial \rho U_i}{\partial t} + \frac{\partial}{\partial x_j}(\rho U_i U_j) = -\frac{\partial p}{\partial x_i} + \frac{\partial}{\partial x_i}\left(\mu_{\text{eff}}\left(\frac{\partial U_i}{\partial x_j} + \frac{\partial U_j}{\partial x_i}\right)\right)$$

and the continuity equation as:

$$\frac{\partial \rho}{\partial t} + \frac{\partial}{\partial x_j}(\rho U_j) = 0,$$

where ρ is the fluid density, p is pressure and μ_{eff} is the effective fluid viscosity. The turbulent eddy viscosity is treated analogously to viscosity in laminar flow such that $\mu_{\text{eff}} = \mu_t + \mu$ where μ_t is the turbulent viscosity and μ the fluid viscosity. The $k-\varepsilon$ model assumes that the local turbulent viscosity is related to the local turbulent kinetic energy (k) and the eddy dissipation rate (ε) as follows:

$$\mu_t \propto \rho \frac{k^2}{\varepsilon}.$$

The advection–diffusion equation for conservative tracers was used to model the transport of the odorant:

$$\partial_t C_x + \mathbf{u} \cdot \nabla C = (D_m + \varepsilon)\nabla^2 C_x,$$

where C_x is the tracer concentration, $\mathbf{u}$ is the velocity field, D_m is the molecular diffusivity and ε is the local eddy diffusivity solved from the turbulence model. For all further analysis, we used the concentration and velocity in a plane 1 mm above the bottom of the domain, in the approximate z-plane of the fly antennae.

Mathematical modelling and data analysis

Inter-antennal latency of edge hit ΔT. The inter-antennal latency ΔT as a function of fly walking speed $|\mathbf{v}_{\text{fly}}|$ and bar speed $|\mathbf{v}_{\text{bar}}|$ can be calculated with basic geometric considerations. Here we assume that the fly speed along the bar direction is sufficiently slow such that the bar passes over the fly. Consider a coordinate system in the frame of the moving bar, where the bar direction is $+y$ (that is, the bar's edge is in x). The fly velocity in this frame is

$$\mathbf{v}_r = [-|\mathbf{v}_{\text{fly}}|\sin\phi,\ |\mathbf{v}_{\text{fly}}|\cos\phi - |\mathbf{v}_{\text{bar}}|],$$

where ϕ is the angle of rotation from $\mathbf{v}_{\text{bar}}$ to $\mathbf{v}_{\text{fly}}$ in the experimenter frame. The inter-antennal latency ΔT is then the projection of the antennal spacing L along $\mathbf{v}_{\text{bar}}$ divided by the projection of $\mathbf{v}_r$ along $\mathbf{v}_{\text{bar}}$. The former is $L\sin\phi$ and the latter is the y-component of $\mathbf{v}_r$; the sign of $L\sin\phi$ is treated as meaningful, so that a positive/negative value means the left/right antenna is hit first. Thus:

$$\Delta T = \frac{L\sin\phi}{|\mathbf{v}_{\text{bar}}| - |\mathbf{v}_{\text{fly}}|\cos\phi},$$

where the sign is given by the numerator since the denominator is always positive for bars passing over the fly.

This expression ignores the fly's angular velocity while walking. Assuming that the fly is walking forward while also turning at a rate ω, then the total accumulation of orientation over the ΔT interval is $\omega\Delta T$, which for typical values of the maximum rotation rate during normal turns ($\omega \approx 300°$ s^{-1}) and typical inter-antennal latencies without turning ($\Delta T \approx 15$ ms) is ~5°. This would be if the fly were turning at a maximum angular velocity. More typically, rotation rates are approximately 20° s^{-1} (ref. [10]), giving an accumulated angle during of less than 1°. If we incorporate this error as an uncertainty on ϕ, $\delta\phi$, then ΔT acquires an error of

$$\delta\Delta T = \delta\phi\left[\frac{L\cos\phi}{|\mathbf{v}_{\text{bar}}| - |\mathbf{v}_{\text{fly}}|\cos\phi} + \frac{|\mathbf{v}_{\text{fly}}|L\sin^2\phi}{(|\mathbf{v}_{\text{bar}}| - |\mathbf{v}_{\text{fly}}|\cos\phi)^2}\right]$$

With the values assumed throughout, $|\delta\Delta T| < 1$ ms, so ω is safely ignored to the resolution of our experiments.

HRC output versus ΔT for travelling edges. Our prediction for the turning bias as a function of the latency ΔT at which an edge of odour hits the right antenna after hitting the left, is based on the output $r(t)$ of a mirror-symmetrized HRC[16]. To calculate $r(t)$, we model the correlator architecture as depicted in Fig. 4a. Specifically, the time-varying signals from the 2 sensors are $s_L(t)$ and $s_R(t)$. In one arm of the computation, $s_L(t)$ is linearly filtered with an exponential $\frac{1}{\tau}e^{-\frac{t}{\tau}}$, while $s_R(t)$ is transmitted unchanged; these are then multiplied. For a travelling ON edge moving left to right, we have $s_L(t) = H(t)$ and $s_R(t) = H(t-\Delta T)$, where H(·) is the Heaviside function. Then, the product of the filtered values is:

$$s_{LR}(t) = H(t-\Delta T)\frac{1}{\tau}\int_{-\infty}^{t} e^{-\frac{t-t'}{\tau}} H(t')\,dt'$$

$$s_{LR}(t) = H(t-\Delta T)\frac{1}{\tau}\int_{0}^{t} e^{-\frac{t-t'}{\tau}} dt'$$

$$s_{LR}(t) = H(t-\Delta T)\left(1 - e^{-\frac{t}{\tau}}\right)$$

The other arm is similar, except that $s_R(t)$ is filtered and $s_L(t)$ is transmitted unchanged. Then the product of the filtered inputs is:

$$s_{RL} = H(t)\frac{1}{\tau}\int_{-\infty}^{t} e^{-\frac{t-t'}{\tau}} H(t'-\Delta T)\,dt'$$

$$= H(t-\Delta T)(1 - e^{-\frac{t-\Delta T}{\tau}}).$$

The correlator output is therefore:

$$r(t) = s_{LR}(t) - s_{RL}(t) = H(t-\Delta T)\left(e^{-\frac{t-\Delta T}{\tau}} - e^{-t/\tau}\right).$$

Assuming that flies sense odour motion using this computation, the output of the correlator, $r(t)$, must be converted to a behaviour; here, we model this behaviour as the turning bias being proportional to $\int r(t)\,dt$:

$$\text{Turning bias} \propto \int_{-T_-}^{T_+} r(t)\,dt = \int_{\Delta T}^{T_+} \left(e^{-\frac{t-\Delta T}{\tau}} - e^{-t/\tau}\right) dt$$

$$\text{Turning bias} \propto \int_{-\infty}^{\infty} r(t)dt \propto \left(1 - e^{-\frac{\Delta T}{\tau}}\right)$$

This second expression is valid provided that behavioural timescales T_- and T_+, over which the correlator response is integrated to produce the turning response, are large compared to both τ and ΔT. Long after the edge hit, $t \gg T_-$, the signals are both $s_L = s_R = 1$, giving an HRC output of 0, as expected for the anti-symmetric architecture.

To estimate the filtering constant τ, we minimize:

$$C(A,\tau) = \left[\text{Turning bias}(\Delta T) - A\left(1 - e^{-\frac{\Delta T}{\tau}}\right)\right]^2$$

over A,τ. The turning bias is plotted in increments of $\Delta T = 4$ ms, where the value at a given ΔT includes values from ±4 ms. Neighbouring points therefore contain overlapping data; this has the effect of smoothing, but not biasing, the turning bias versus ΔT curve.

Responses to rightward-moving OFF edges are analogous. The signal switches from 1 to 0 at the OFF edge (set it to $t = 0$), so the signal on the left sensor is $s_L(t) = 1 - H(t)$ and for the right sensor is $s_R = 1 - H(t - \Delta T)$. Then, one arm of the HRC is:

$$s_{LR}(t) = (1 - H(t - \Delta T))\frac{1}{\tau}\int_{-\infty}^{t} e^{-\frac{t-t'}{\tau}}(1 - H(t'))dt'$$

$$s_{LR}(t) = (1 - H(t - \Delta T))\frac{1}{\tau}\int_{-\infty}^{0} e^{-\frac{t-t'}{\tau}}dt',\ t > 0$$

$$s_{LR}(t) = e^{-\frac{t}{\tau}},\ 0 < t < \Delta T$$

and $s_{LR}(t) = 0$ for $t > \Delta T$ and $s_{LR}(t) = 1$ for $t < 0$. The other arm output is simply $s_{RL} = 1$ for $t < 0$ and $s_{RL} = 0$ for $t > 0$, as the non-delayed arm drops to zero as soon as the edge passes it at $t = 0$. Thus, the output is:

$$r(t) = s_{LR}(t) - s_{RL}(t) = e^{-\frac{t}{\tau}}H(t)(1 - H(t - \Delta T))$$

Integrating this quantity over time gives the same turning bias as the ON edge.

Generation of correlated noise stimuli and $C(\Delta x,\Delta t)$. Correlated noise stimuli were generated as previously described[26]. We used optogenetic bars that were parallel to the short axis (y) of the arena (for example, perpendicular to the wind direction, which runs along x). Each bar has a width of one x-pixel; thus, we refer to an x-pixel as a pixel, as correlations are defined just in the x-direction. The stimulus value (where −1 and 1 are for dark and light bars, respectively) of a bar at pixel location x and time t is given by $c(x,t) = \text{sgn}(\eta(x,t) + \alpha\eta(x + \beta\Delta x, t + \Delta t))$, where each value of the random field $\eta(x,t)$ is independently chosen from a standard normal distribution. Δx is the pixel spacing; Δt is the interframe interval. The constant β governs the direction of the correlations: +1 for stimuli correlated in the $+x$ direction (with-wind in the main text) and −1 for stimuli correlated in the $-x$ direction (against-wind). The constant α governs the polarity of the correlations; +1 or −1 for positive or negative correlations, respectively.

The spatiotemporal correlations in pixel intensity can be computed in a straightforward manner, as previously described[26]. Assume that $\alpha = \beta = 1$; the other cases are analogous. The correlation between two pixels separated by spacing x' and timing t' is denoted by the correlation function $C(x',t') = \langle c(x,t)c(x + x', t + t')\rangle$. In general,

$$C(x', t') = \langle \text{sgn}((\eta_1 + \eta_2)(\eta_3 + \eta_4))\rangle,$$

where η_i is one sample of η. For most choices of t', x', all η_i are distinct, so the correlation reduces to 0 as the sums are independent. For $x' = t' = 0$, the correlation reduces to the variance of $c(x,t)$, which is 1. However, for $t' = \Delta t$ and $x' = \Delta x$, $\eta_2 = \eta_3$. Then,

$$C(x', t') = \langle \text{sgn}((\eta_1 + \eta_2)(\eta_2 + \eta_4))\rangle$$

$$C(x,\ t) = \langle \text{sgn}((\eta_1 - \eta_2)(\eta_2 - \eta_4))\rangle$$

as the random variables are symmetric about 0. The sign depends only on the ordering of the η_i, which are 3 independent samples from a standard normal distribution. There are 6 ways to uniquely order the η_i, only two of which give a positive sign ($\eta_1 > \eta_2 > \eta_4$ and $\eta_1 < \eta_2 < \eta_4$); thus, the expected value is 1/3 (ref. [26]). An analogous property holds for $t' = -\Delta t, x' = -\Delta x$. Finally, the α and β factors are incorporated in a straightforward manner as scale factors, giving:

$$C(x', t') = \delta_{x',0}\delta_{t',0} + \alpha\frac{1}{3}(\delta_{x',\beta\Delta x}\delta_{t',\Delta t} + \delta_{x',-\beta\Delta x}\delta_{t',-\Delta t}),$$

where the δ denotes the Kronecker delta function. Note that the correlation can be calculated by averaging over all of spacetime, or just in space for a fixed set of times, or just in time for a fixed set of points. The latter is our interpretation for the HRC output from fixed antennae, assuming the correlation direction is perpendicular to the fly body.

Generation of glider stimuli. Here, the stimulus value of a bar at pixel location x and time t is given by $c(x,t) = B(x - \beta t\Delta x/\Delta t)$, where $B = 2X - 1$ with $X \approx \text{Bernoulli}(p = 0.5)$, Δx is the pixel spacing and Δt is the interframe interval. The correlation between two pixels separated by spacing x' and timing t' is

$$C(x', t') = \left\langle \left[B\left(x - \frac{\beta t\Delta x}{\Delta t}\right)B\left(x + x' - \frac{\beta t\Delta x}{\Delta t} - \frac{\beta t'\Delta x}{\Delta t}\right)\right]\right\rangle.$$

Then, $C(x',t') = 1$ when $\frac{x'}{t'} = \frac{\beta\Delta x}{\Delta t}$, that is, the correlation matrix has a diagonal or antidiagonal structure for $\beta = 1$ and $\beta = -1$, respectively. These stimuli are a class of glider stimuli with a two-point correlation structure[32,33]. Visually, these gliders are a frozen pattern of random light and dark bars moving at constant speed in the βx direction.

HRC output for correlated noise stimuli. Here we calculate the HRC output for correlated noise stimuli, which has been computed before for any pair of filters on the two arms of the HRC[26,55]. Assume that the antennae are held at approximately the spacing of the correlation shift Δx (see the 'Generation of correlated noise stimuli and $C(\Delta x,\Delta t)$' section), and that the correlation direction is $+x$ (rightward over the fly body), so $\beta = 1$ from the last section. Then, one arm of the HRC gives:

$$s_{LR}(t) = s_R(t)\frac{1}{\tau}\int_{-\infty}^{t} e^{-\frac{t-t'}{\tau}}s_L(t')dt'.$$

Averaging over time gives:

$$\langle s_{LR}(t)\rangle = \langle c(x,t)\frac{1}{\tau}\int_{-\infty}^{t} e^{-\frac{t-t'}{\tau}}c(x - \Delta x, t')dt'\rangle.$$

As $\beta = 1$, then only the last term in the correlation equation applies:

$$\langle s_{\mathrm{LR}}(t)\rangle = \langle c(x,t)\frac{1}{\tau}\int_{-\infty}^{0} \mathrm{e}^{t''/\tau} c(x-\Delta x, t+t'')\mathrm{d}t''\rangle$$

$$\langle s_{\mathrm{LR}}(t)\rangle = \frac{1}{\tau}\int_{-\infty}^{0} \mathrm{e}^{t''/\tau}\alpha\frac{1}{3}\delta_{t'',-\Delta t}\mathrm{d}t''$$

$$\langle s_{\mathrm{LR}}(t)\rangle = \alpha\frac{1}{3\tau}\mathrm{e}^{-\Delta t/\tau},\ \Delta t>0.$$

This equation holds for Δt being positive. The other arm is analogous, for $\Delta t<0$.

$$s_{\mathrm{RL}}(t) = s_{\mathrm{L}}(t)\frac{1}{\tau}\int_{-\infty}^{t} \mathrm{e}^{-\frac{t-t'}{\tau}} s_{\mathrm{R}}(t')\,\mathrm{d}t'$$

$$\langle s_{\mathrm{RL}}(t)\rangle = \langle c(x,t)\frac{1}{\tau}\int_{-\infty}^{t} \mathrm{e}^{-\frac{t-t'}{\tau}} c(x+\Delta x, t')\mathrm{d}t'\rangle$$

$$\langle s_{\mathrm{RL}}(t)\rangle = \langle c(x,t)\frac{1}{\tau}\int_{-\infty}^{0} \mathrm{e}^{\frac{t''}{\tau}} c(x+\Delta x, t+t'')\mathrm{d}t''\rangle$$

$$\langle s_{\mathrm{RL}}(t)\rangle = \frac{1}{\tau}\int_{-\infty}^{0} \mathrm{e}^{\frac{t''}{\tau}}\alpha\frac{1}{3}\delta_{t'',\Delta t}\mathrm{d}t''$$

$$\langle s_{\mathrm{RL}}(t)\rangle = \alpha\frac{1}{3\tau}\mathrm{e}^{\Delta t/\tau},\ \Delta t<0$$

Thus, the full correlator output is

$$\int_t r(t)\mathrm{d}t = \langle s_{\mathrm{LR}}(t)\rangle - \langle s_{\mathrm{RL}}(t)\rangle = \alpha\ \mathrm{sgn}(\Delta t)\frac{1}{3\tau}\mathrm{e}^{-\frac{|\Delta t|}{\tau}}$$

Note that the correlator output response switches sign if the correlation polarity α flips, this is the reverse phi response. There is a slight artificiality in this expression, in that the response is discontinuous at $\Delta t = 0$. We have assumed an exponential filter, which technically has an immediate response time, violating causality. Moreover, the optimal response occurs for an inter-frame interval Δt that is arbitrarily small. As a more realistic filter, one can use $\frac{t}{\tau^2}\mathrm{e}^{-t/\tau}$, which has zero response at time zero and maximal response at $t=\tau$. Then,

$$\int_t r(t)\mathrm{d}t = \langle s_{\mathrm{LR}}(t)\rangle - \langle s_{\mathrm{RL}}(t)\rangle = \alpha\ \mathrm{sgn}(\Delta t)\frac{1}{3\tau^2}|\Delta t|\mathrm{e}^{-\frac{|\Delta t|}{\tau}}$$

This filter is continuous at $\Delta t = 0$, and the maximum correlator output occurs when the filter timescale τ matches the interframe interval Δt. In either case, the salient point is that the response is antisymmetric in both the temporal shift Δt and the correlation polarity α, as expected.

HRC response for prefiltered inputs. Here, we motivate how filtering of inputs affects the response curve of the HRC, that is, HRC output as a function of stimulus latency ΔT. We assume delta-correlated stimuli (as in the 'Generation of correlated noise stimuli and $C(\Delta x,\Delta t)$' section), for which the response functions are expressed in simple, interpretable forms. Thus, we set cross-correlation between the left antennal stimulus and right antennal stimulus at $c(t') = \langle s_{\mathrm{L}}(t)s_{\mathrm{R}}(t-t')\rangle = \delta(t'-\Delta T)$, where the average is taken over instantiations of the stimulus, which is equivalent in this case to taking an average over time. Defining f_1 and f_2 as the delay filters for the two arms (for example, 1 fast and 1 slow filter) and in the absence of any other filters, the averaged HRC output from 1 side of the detector is:

$$s_{\mathrm{LR}}(\Delta T) = \langle \int \mathrm{d}t' f_1(t') s_{\mathrm{L}}(t-t') \int \mathrm{d}t'' f_2(t'') s_{\mathrm{R}}(t-t'')\rangle$$

$$= \int \mathrm{d}t'\mathrm{d}t'' f_1(t') f_2(t'')\delta(t'-t''-\Delta T)$$

$$= \int \mathrm{d}t' f_1(t') f_2(t'-\Delta T)$$

$$= \left(f_1 \otimes f_2\right)(\Delta T).$$

In other words, the response is the convolution of the two filters. Further assuming that $f_2(t)$ is fast (that is, a delta function response), this reduces to the slow filter evaluated at the inter-antennal latency:

$$s_{\mathrm{LR}}(\Delta T) = f_1(\Delta T).$$

Note that this and related derivations (and interpretations) have been given in previous studies[26,55].

Now, assuming that the signals are each prefiltered with a smoothing filter $f_3(t)$, we get:

$$s_{\mathrm{LR}}(\Delta T) = \langle \int \mathrm{d}t'\mathrm{d}t'' f_1(t'-t'') f_3(t'') s_{\mathrm{L}}(t-t') \int \mathrm{d}t'''\mathrm{d}t'''' f_2(t'''-t'''') f_3(t'''') s_{\mathrm{R}}(t-t''')\rangle_t$$

$$= \int \mathrm{d}t'\mathrm{d}t''\mathrm{d}t'''\mathrm{d}t'''' f_1(t'-t'') f_3(t'') f_2(t'''-t'''') f_3(t'''')\delta(t'''-t'-\Delta T)$$

$$= \int \mathrm{d}t'\mathrm{d}t''\mathrm{d}t'''' f_1(t'-t'') f_3(t'') f_2(t'+\Delta T-t'''') f_3(t'''')$$

$$= \int \mathrm{d}t''\mathrm{d}t'''' f_1(t'-t'') f_2(t'+\Delta T-t'''')(f_3\otimes f_3)(t''-t'''')$$

$$= \int \mathrm{d}t''\mathrm{d}t''''(f_1\otimes f_2)(\Delta T-t''''+t'')(f_3\otimes f_3)(t''-t'''')$$

$$= \left(f_1\otimes f_2\right)\otimes\left(f_3\otimes f_3\right)(\Delta T).$$

Again, if f_2 is a delta function response, this gives:

$$s_{\mathrm{LR}}(\Delta T) = f_1 \otimes (f_3 \otimes f_3)(\Delta T).$$

The full HRC response is this quantity, anti-symmetrized:

$$\mathrm{HRC}(\Delta T) = s_{\mathrm{LR}}(\Delta T) - s_{\mathrm{LR}}(-\Delta T)$$
$$= f_1 \otimes (f_3 \otimes f_3)(\Delta T) - f_1 \otimes (f_3 \otimes f_3)(-\Delta T).$$

Thus, the HRC response is essentially the slow filter convolved with the autocorrelation of the prefilter. Indeed, the effect of the prefilter, a linear operation, is to 'smear out' the HRC response—although it acts twice, once for the right sensor and once for the left sensor.

What effect does prefiltering have on the HRC response? As the HRC is defined anti-symmetrically in ΔT, it is direction selective by construction, so the prefiltering will not affect direction selectivity. However, filtering can affect the signal-to-noise ratio and, therefore, the regime for which direction selectivity is resolvable given the noise. For concreteness, let us calculate the closed-form HRC response, assuming that the slow filter and prefilter are each exponential filters with timescales τ_{HRC} and τ_{smear}, respectively, and assuming that there is noise in the external signal. We are considering binary valued correlated signals, so we imbue the noise as a random variable that adds external variability to the timing of the signals. As we are looking at antenna-to-antenna correlations, we add the noise to just one antenna for simplicity.

In the prior derivation, noise changes the integrated time t''' to $t''' + X$, where we take $X \approx N(0,\delta t)$ as the noise. Then, the noisy HRC response is:

$$\begin{aligned}\mathrm{HRC}(\Delta T|\delta T) &= s_{\mathrm{LR}}(\Delta T - X) - s_{\mathrm{LR}}(-\Delta T + X)\\ &= f_1 \otimes (f_3 \otimes f_3)(\Delta T - X)\\ &\quad - f_1 \otimes (f_3 \otimes f_3)(-\Delta T - X)\end{aligned}$$

In other words, the noise simply manifests as $\Delta T \to \Delta T - X$ in the HRC response. We thus just designate $\Delta T_{\delta T} = \Delta T + X$ as a normal random variable with mean ΔT and standard deviation δT.

Now, the autocorrelation of an exponential pre-filter is:

$$(f_3 \otimes f_3)(t) = \frac{1}{\tau_{\mathrm{smear}}^2} t \mathrm{e}^{-\frac{t}{\tau_{\mathrm{smear}}}} H(t)$$

and therefore the response of 1 arm of the noisy HRC gives:

$$s_{\mathrm{LR}}(\Delta T_{\delta t}) = \frac{1}{\tau_{\mathrm{HRC}} \tau_{\mathrm{smear}}^2}\left(-\frac{\Delta T_{\delta t}}{\lambda^*}\mathrm{e}^{-\frac{\Delta T_{\delta t}}{\tau_{\mathrm{smear}}}} + \frac{1}{\lambda^{*2}}(\mathrm{e}^{-\frac{\Delta T_{\delta t}}{\tau_{\mathrm{HRC}}}} - \mathrm{e}^{-\frac{\Delta T_{\delta t}}{\tau_{\mathrm{smear}}}})\right) H(\Delta T_{\delta t}),\ \tau_{\mathrm{HRC}} \neq \tau_{\mathrm{smear}}$$

$$s_{\mathrm{LR}}(\Delta T_{\delta t}) = \frac{1}{2\tau_{\mathrm{HRC}}^3}(\Delta T_{\delta t})^2 \mathrm{e}^{-(\Delta T_{\delta t})/\tau_{\mathrm{HRC}}} H(\Delta T_{\delta t}),\ \tau_{\mathrm{HRC}} = \tau_{\mathrm{smear}},$$

where $\lambda^* = \frac{1}{\tau_{\mathrm{smear}}} - \frac{1}{\tau}$. Again, the full response is $\mathrm{HRC}(\Delta T_{\delta t}) = s_{\mathrm{LR}}(\Delta T_{\delta t}) - s_{\mathrm{LR}}(-\Delta T_{\delta t})$. We then define the minimum resolvable ΔT as:

$$\Delta T_{\mathrm{resolvable}}(\delta t) = \min|\Delta T| \ \text{ s.t. } \langle \mathrm{HRC}(\Delta T_{\delta t})\rangle_X > \sqrt{\langle \mathrm{HRC}(\Delta T_{\delta t})^2\rangle_X - \langle \mathrm{HRC}(\Delta T_{\delta t})\rangle_X^2}$$

In words, it is, for a given noise level δt, the minimum inter-antennal latency ΔT for which the mean of the response is larger than the s.d. of the responses. In realistic scenarios, the negative responses for $\Delta T_{\delta t} < 0$ can mix with the positive responses for $\Delta T_{\delta t} > 0$, confounding responses for ΔT near 0, and our interest here is the magnitude of this effect. We calculate $\Delta T_{\mathrm{resolvable}}(\delta t)$ numerically for the two-exponential response given the above expressions (Extended Data Fig. 6) for various values of τ_{smear}. We find that the minimum resolvable ΔT is limited entirely to the noise level δt, regardless of whether τ_{smear} is much larger or much smaller than τ_{HRC}. This indicates that the prefilter certainly affects the values of the HRC output, but it does not affect the direction-sensing abilities of the HRC.

Calculated HRC responses from electrophysiological measurements. To estimate HRC outputs from a pair of recorded ORN spike trains, we first manually shifted one recording from the pair by $-\Delta T/2$ and the other by $\Delta T/2$, which mimics an odour edge travelling from left to right, hitting the two antennae sequentially at a latency of ΔT. The magnitude of ΔT is inversely proportional to the odour speed; assuming an interantennal distance of 300 μm, the corresponding odour speed is $300/\Delta T$ μm s^{-1}. Leftward-travelling odours are simulated by choosing $\Delta T < 0$. We first produce ORN firing rates from these spike trains by convolving the binary spike trains with a Gaussian filter ($\sigma = 15$ ms). HRC outputs were generated from these firing rates using the procedure described in the above sections, choosing a $\tau = 15$ ms exponential filter for the delay arm.

For the scenario in which we added multiple sources of noise (Fig. 5e), we first took the recorded spike trains and shifted each spike by τ_{jitter}, where τ_{jitter} was chosen uniformly from −30 to 30 ms. Next, these spikes were shifted by $\pm\Delta T/2$ as above, to assign left and right ORNs, and then filtered in time as above to get ORN firing rates $r_{\mathrm{ORN,L}}(t)$ and $r_{\mathrm{ORN,R}}(t)$. Left and right projection neurons receive input from both ORNs, but with differing weights[17], which we mimicked by taking the input to the left projection neuron $r_{\mathrm{PN\,in,L}}(t) = 0.6\, r_{\mathrm{ORN,L}}(t) + 0.4\, r_{\mathrm{ORN,R}}(t)$ and $r_{\mathrm{PN\,in,R}}(t) = 0.6\, r_{\mathrm{ORN,R}}(t) + 0.4\, r_{\mathrm{ORN,L}}(t)$. Projection neurons average over many ORN inputs by filtering over 30 ms (ref. [34]), which we mimicked by designating the projection neuron response as $r_{\mathrm{PN,L}} = f_{\mathrm{PN}} \otimes r_{\mathrm{PN\,in,L}}$, where $f_{\mathrm{PN}}(t)$ is a 30 ms exponential filter. Finally, $r_{\mathrm{PN,L}}$ and $r_{\mathrm{PN,R}}$ were used as inputs to the HRC described above.

Analysis of imaged plume. We reanalysed behavioural data previously extracted from *Drosophila* navigating an imaged complex plume of smoke[10] in the same walking assay used throughout this study. The signal in the virtual antenna was quantified as described previously; in brief, the virtual antenna is defined as an ellipse perpendicular to the body axis with the long axis given by the width of the fly (1.72 ± 0.24 mm) and the small axis equal to one-fifth the minor axis of the fly (0.46 ± 0.24 mm). We reanalysed the imaged fly and signal data to resolve the virtual antenna signal into 14 pixels along its long axis (averaged along its short axis). Thus, the signal is a vector $\mathbf{s}_{\mathrm{ant}}(t) = [s(x_1,t), s(x_2,t), \ldots, s(x_{14},t)]$ defined at locations along the antenna's long axis $\mathbf{x}_{\mathrm{ant}} = [x_1, \ldots, x_{14}]$ for a given time t.

The overall concentration in the antenna was calculated as the average signal over the centre of the virtual antenna, at the locations $[x_5,x_6,x_7,x_8]$. The gradient ∇c_{ant} in the virtual antenna at a given t was calculated by regressing $\mathbf{s}_{\mathrm{ant}}$ against $\mathbf{x}_{\mathrm{ant}}$ and extracting the slope. The odour velocity in the virtual antenna was estimated by calculating correlations of the virtual antenna signal over space and time. For a given t, we calculated $\widehat{\Delta x} = \mathrm{argmax}_{\Delta x}\langle s(x_i,t)s(x_i+\Delta x, t+\Delta t)\rangle_{x_i}$, where Δx spanned integers from −7 to 7, and Δt is the interframe interval (11 ms), and $s(\cdot)$ were mean subtracted. This gives the signed number of pixels for which the correlation between two successive frames is maximized, up to the length of the antenna. The odour velocity was then defined as $\widehat{\Delta x}$ × frame rate×resolution, where the imaging frame rate was 90 frames per second and the spatial resolution is 0.153 mm per pixel. We disregarded points for which $\widehat{\Delta x}$ was ±7, as those may not represent local maxima but were instead limited by the size of the antenna. All three quantities—total concentration, gradient and odour velocity—were smoothed in time using a Savitsky–Golay filter of order 2 and a smoothing window of 21 timepoints (~350 ms).

To remove boundary effects from the arena extent, we used for Fig. 1c–e only points for which the fly was in the central region of the arena, $100 < x < 250$ mm, $|y - y_0| < 40$ mm, where y_0 is the plume's central axis, and only points for which fly speed was greater than 0.1 mm s^{-1}. Angular velocity was calculated as the average orientation change over 200 ms.

Analysis of simulated plume. The simulation generated concentration fields $c(x_i,y_i,t)$ and flow velocity fields $\mathbf{v}_{\mathrm{wind}}(x_i,y_i,t)$ defined on grid points (x_i,y_i) of a non-uniform mesh. We first generated values on a 0.5 mm square lattice, by triangulating the data and performing barycentric linear interpolation over each triangle (scipy.interpolate.griddata in Python, with the method 'linear'). Fields in Fig. 6 and Extended Data Fig. 7 were plotted every 1 cm, (that is, every 20 pixels on the original 0.5 mm lattice). Wind speed vectors at each point on this 1 cm lattice were generated by averaging $\mathbf{v}_{\mathrm{wind}}$ over the 20 × 20 values in a 1 cm^2 box. The plotted $\mathbf{v}_{\mathrm{wind|odour}}$ field was generated by considering only wind vectors for which the odour concentration was above 1×10^{-3}. Odour gradients were generated by calculating local differences ∇c_x and ∇c_y in the x and y directions, respectively. Specifically, for ∇c_x, we calculated $(c(x_+) - c(x_-))/(c(x_+) + c(x_-))$, where x_+ and x_- were the averages in the right and left half of a 1 cm^2 box centred at each lattice point, respectively. ∇c_y was calculated analogously, using the top and bottom half of the same box. Odour velocities were calculated similarly to those in the imaged plume used in Fig. 1, by correlating the values in a given spatial region between two frames. Specifically, to get $\mathbf{v}_{x,\mathrm{odour}}$ at a given time t, we calculated $\mathrm{argmax}_{\Delta x}\langle s(x_j,t)\, s(x_j+\Delta x, t+\Delta t)\rangle_{x_j}$ where $s(x_j,t)$

was the odour concentration in a 1 cm^2 box averaged over the y direction for each x_j pixel spaced by 0.5 mm. The shifts Δx ran from −20 to 20 pixels (±1 cm). This quantity was multiplied by the frame rate of 100 frames per second and by the spatial resolution 0.5 mm per pixel to get $\mathbf{v}_{x,\mathrm{odour}}$ in mm s^{-1}. An analogous operation was performed for $\mathbf{v}_{y,\mathrm{odour}}$ using the same 1 cm^2 box. All odour gradient and odour velocity values for very low odour concentrations were set to Nan, as were any odour velocity values that produced a maximum shift $|\Delta x| = 20$. The resulting wind speed, gradient and odour velocity were all smoothed in time using a Savitsky–Golay filter of order 1 and window length 11 (110 ms).

Analysis of fly navigation in complex virtual plumes. For the plume navigation experiments (Extended Data Fig. 7), we considered tracks that began in the downwind 50 mm of the arena ($x > 230$ mm) and had an average walking speed of at least 0.5 mm s^{-1}. For the histograms (Fig. 6f,i (middle and right plots)), we only plotted instances at which the fly's instantaneous walking speed was greater than 5 mm s^{-1}. For the success ratios (Fig. 6f,i (left plots)), we considered tracks that lasted 30 s or longer, or that reached the upwind end of the arena ($x < 50$ mm) before then.

In silico virtual agent model and simulation. We used two different navigation algorithms for the agent-based simulations.

The bio-inspired algorithm (Fig. 6j–l) was modelled on our previous work[10], which quantified the navigational behaviour of walking *Drosophila* in spatiotemporally complex odour plumes. We ran the agents in the imaged complex plume used in the plume navigation experiments (Fig. 6g). We recapitulate the algorithm briefly here, but refer the reader to the original study for all details.

We generated two types of agents: DS− agents, which obeyed the original navigational model and could not sense odour direction, and DS+ agents, which combined the original model with odour-direction sensing. Both DS+ and DS− agents navigated using the timing of odour hits—times at which $c(t)$ exceeded a threshold, here chosen to be 3 (the digitized signal ranges from 0 to 255). At each frame, agents underwent stochastic transitions between walking, turning and stopped states. Agents walked at a constant speed of 10 mm s^{-1}. During walking, their heading underwent rotational diffusion, with a s.d. of 0.22° every frame (each frame is 1/60 s). Transitions from a stopped to walking state were inhomogeneous Poisson processes, in which the transition rate increased monotonically with the frequency of odour hits. Transitions from walking to a stopped state were also inhomogeneous Poisson processes, whereby the rate dipped at each odour hit, before decaying back to a baseline; thus, flies keep walking when the frequency of odour hits is high. Turns occurred only while walking, and were Poisson events with a rate of 0.5 Hz. Each turn magnitude was a random sample from $N(30°,8°)$.

The key navigational aspect of the bio-inspired algorithm was the turn direction. For DS− agents, the turn direction was a binary random variable, either upwind or downwind, where $p(\mathrm{upwind}) = \min(1, 0.5 + \alpha w(t))$, where $\alpha = 1$ and $w(t)$ is a running average of the frequency of odour hits. As in the original study, the running average is computed by convolving the binary vector of odour hit onsets (1 at the onset of each odour hits; 0 elsewhere) with an exponential filter of timescale 2 s. Thus, for frequent odour hits, the turns are more likely to be directed upwind. For DS+ agents, the turn direction was a binary variable, either against or towards $\mathbf{v}_{\mathrm{sum}}$, where $\mathbf{v}_{\mathrm{sum}}$ is the vector sum of the odour motion direction and wind direction: $p(\mathrm{against}) = \min(1, 0.5 + \alpha w(t))$, where $\alpha = 1$. Thus, as the frequency of the odour hits increases, the agent is more likely to direct its turns against the summed direction $\mathbf{v}_{\mathrm{sum}}$.

To compute the odour hit times (for both DS− and DS+ agents) and odour direction (for only DS+ agents), the agents had two antennae separated by 1.5 mm, and each antennae received an odour signal, $c_L(t)$ and $c_R(t)$, respectively, that was the average signal value in a 0.5 × 0.5 mm^2 region. The total odour signal $c(t)$ was $\frac{c_L(t) + c_R(t)}{2}$. For DS+ agents, the odour motion direction was computed by taking the sign of $c_{\mathrm{odour}}(t) = c_L(t)c_R(t + \Delta T) - c_L(t + \Delta T)c_R(t)$, where the delay ΔT was chosen as 1 time frame. For $c_{\mathrm{odour}}(t) > 0$, odour direction vector pointed $\theta + 90°$, and for $c_{\mathrm{odour}}(t) < 0$, odour direction vector pointed $\theta - 90°$, where θ is the agent heading. In other words, the agent can resolve only the direction, left or right, of the odour motion. If the correlation magnitude is too low ($|c_{\mathrm{odour}}| < 5$), then DS+ agents ignore c_{odour} and turn against the wind direction like DS− agents.

All 100 agents in the bio-inspired algorithm were initialized in the back 50 mm of the arena and uniformly in the lateral direction, and their headings were initialized randomly in the upwind 180 sector. Agents were simulated for 2,500 frames, or 41.7 s. If agents reached the rectangular boundary of the arena, they were reflected ballistically from the wall.

In the simple algorithm (Extended Data Fig. 9), virtual agents with 2 spatially separated sensors navigated the simulated plume (Fig. 6a) using a simple algorithm. All agents were initialized at the back of the arena, facing upwind. At each frame (10 ms), agents turned either left or right 90° (except for upwind oriented DS− flies when within the odour signal—these flies maintained upwind), depending on the navigation strategy as described in the main text, and stepped forwards 0.75 mm. The sensors were placed 0.5 mm to the left or right of the agent centroid. The measured odour signal concentration was defined as $c = \frac{(c_L + c_R)}{2}$, where the concentration in each sensor was c_L and c_R, respectively. We set the detection threshold at $c_0 = 1 \times 10^{-3}$. The odour correlation between the two sensors was defined as $c_{\mathrm{odour}}(t) = c_L(t)c_R(t + \Delta T) - c_L(t + \Delta T)c_R(t)$, where the delay timescale ΔT was chosen as 1 frame (1/100 s). From c_{odour}, the direction of odour motion v_{odour} was defined as +1 if $\mathrm{abs}(c_{\mathrm{odour}}(t)) > 1 \times 10^{-8}$ and $\mathrm{sgn}(c_{\mathrm{odour}}(t)) > 0$; as −1 if $\mathrm{abs}(c_{\mathrm{odour}}(t)) > 1 \times 10^{-8}$ and $\mathrm{sgn}(c_{\mathrm{odour}}(t)) < 0$; and as 0 otherwise. In general, odour signals with a leftward component over the virtual agent in its body frame had $v_{\mathrm{odour}} = 1$, while those with a rightward component had $v_{\mathrm{odour}} = -1$. Simulations were carried out separately for agents that could sense (DS+) and could not sense (DS−) odour motion. Agents followed the strategy as described in the main text. For DS+ flies, whenever c_{odour} was below the threshold ($\mathrm{abs}(c_{\mathrm{odour}}(t)) > 1 \times 10^{-8}$), but the odour was still detectable ($c > c_0$), the decisions obeyed the DS− strategy. All agents were initialized in the back 50 mm of the arena and uniformly in the crosswind direction, and simulated for 2,500 timesteps, or 25 s.

Theoretical analysis of odour motion in turbulent odour plumes. Here we investigated the motion of odour signals perpendicular to the mean flow using a toy model of turbulent plume similar in spirit to those used in refs. [19,56,57]. Odour packets are released from a point source at a given rate. The concentration around the centre of each packet is given by a local diffusive process that spreads the concentration through molecular diffusion of the odour. Meanwhile, the packets themselves are advected downwind by the mean flow, while being dispersed by the fluctuating velocity u (ref. [19]). We consider the simple case of an isolated packet and calculate its expected velocity crosswind to the flow, at different locations throughout the plume. For analytical simplicity, we assume stationary homogeneous and isotropic turbulence and model the turbulent velocity u as a telegraph process that switches between left motion and right motion at speed v, where the switching rates from left to right and vice versa are both $\lambda = 1/T$. Thus, $2T$ is equivalent to the Lagrangian integral time scale and the packet speed v to the r.m.s. of the turbulent velocity field. While the velocity u switches discontinuously between $+v$ and $-v$, its time correlation function is the same as that of the Ornstein–Uhlenbeck process often used to model homogeneous isotropic turbulence[19,54]:

$$\langle u(t)u(t')\rangle \propto \mathrm{e}^{-\frac{|t-t'|}{2T}}.$$

Our goal is an estimate of the average odour motion velocity at a given lateral distance from the plume, at a given time t, $\langle v\rangle_{y,t}$. As packets are advected downwind at some speed $U \gg v$, we have $t \approx x/U$, so that

this is equivalent to finding the average lateral velocity at some x,y position in the plume[54]. Run times are distributed as $\frac{1}{T}e^{-t/T}$, so packets reaching a given y will have been travelling for some distance $\tilde{y}$, where $\tilde{y}$ is distributed as $p(\tilde{y}) = \frac{1}{Tv}e^{-\tilde{y}/Tv}$. If the packets were originally uniformly distributed, then the average velocity at y would be 0. However, an asymmetry arises due to the non-uniform packet distribution, which is dispersing laterally from a delta function at $y = 0$. For times $t \gg T$, the distribution of packets is approximately the diffusion kernel with effective turbulent diffusivity $D_T = Tv^2$:

$$p(y,\ t) = \frac{1}{\sqrt{2\pi Tv^2 t}}e^{-y^2/2Tv^2 t}$$

Under these assumptions, the average velocity at the fixed point $\langle v\rangle_{y,t}$ is:

$$\langle v\rangle_{y,t} = \frac{v\int_{-\infty}^{y} p(y',\ t-y'/v)e^{-\frac{y-y'}{vT}}dy' - v\int_{y}^{\infty} p(y',t-y'/v)e^{-\frac{y'-y}{vT}}dy'}{\int_{-\infty}^{\infty} p(y',t-y'/v)e^{-\frac{|y-y'|}{vT}}dy'}$$

The first term in the numerator is for packets reaching y that have come from its left (these are travelling in the $+y$ direction), while the second is for those reaching y that have come from the right, which are travelling in the $-y$ direction. The denominator is a normalization factor given by the total number of packets reaching y at time t. This equation can be integrated numerically. To obtain an analytical approximation, we neglect the change in the packet distribution over the time of travelling one correlation time, approximating $p(y',t-y'/v)$ by $p(y',t)$, as the packet distribution does not change appreciably over that time (the validity of this assumption was verified by simulations). Integrating:

$$\langle v\rangle_{y,t} = v\frac{(R_+ - R_-)}{(R_+ + R_-)},$$

where

$$R_+ = e^{\frac{y}{Tv}}\left(1 - \mathrm{erf}\frac{vt+y}{\sqrt{2Tv^2 t}}\right)$$

$$R_- = e^{-\frac{y}{Tv}}\left(1 - \mathrm{erf}\frac{vt-y}{\sqrt{2Tv^2 t}}\right)$$

for $|y| < vt$, and 0 otherwise. We are interested in (1) whether the average lateral velocity of the packets is directed outward from the plume, which would be indicated by an asymmetrical dependence in y, and (2) how this asymmetry depends on the correlation time T. The profile of $\langle v\rangle_{y,t}$ is odd for all T (Extended Data Fig. 10a), indicating that, for any T, the velocity of odour packets in the crosswind direction points away from the plume's central axis. Moreover, for higher T, the velocity component points more strongly outward through a larger portion of the plume, indicating that correlations in the packet motion underlie this directional cue (Extended Data Fig. 10a).

We next investigate how the combination of packet diffusion and packet centroid motion together can influence a spacetime correlation of the odour concentration, as would be computed by time-resolved bilateral measurements. For simplicity, we do this computation in one dimension, considering diffusion of packets and dispersion of their centroids in the y direction only, along with ballistic transport in the x direction. We start with a single packet. Assuming that $y_i(t)$ is the trajectory of the centroid of the packet and $\phi(y,t,|y_i(t)) = \frac{1}{\sqrt{4\pi D_p t}}e^{-(y-y_i)^2/4D_p t}$ is the local concentration at a given location y and time t around the packet. We define the correlator as:

$$C(\Delta y, \Delta t|y,t,y_i(t)) = \phi_{++}\phi_{--} - \phi_{+-}\phi_{-+},$$

where

$$\phi_{++} = \phi(y + \Delta y/2,\quad t + \Delta t/2|y_i(t))$$

$$\phi_{--} = \phi(y - \Delta y/2,\quad t - \Delta t/2|y_i(t))$$

$$\phi_{+-} = \phi(y + \Delta y/2,\quad t - \Delta t/2|y_i(t))$$

$$\phi_{-+} = \phi(y - \Delta y/2,\quad t + \Delta t/2|y_i(t))$$

Thus, the correlator $C(\Delta y,\Delta t|y,t,y_i(t))$ is a time-antisymmetrized quantity, which at time t and position y computes the correlation of the odour concentration between two points in the direction perpendicular to the mean wind, separated by Δy at times separated by Δt, given a packet of which the centre is at (x_i,y_i) and which was released at $t = 0$. We stress that we do not imply that this correlator is being enacted by any circuitry, nor is it a unique definition. However, it has key features—namely, comparisons across space and time and time anti-symmetry—that we will show to be sufficient to detect the lateral odour velocity. Expanding this correlator gives

$$C\left(\Delta y, \Delta t|y,t,y_i(t)\right) = \Delta y\Delta t\left(\phi\partial_t\partial_y\phi - \partial_y\phi\partial_t\phi\right)$$

to the lowest order. For the packet model, at appreciable times $t \gg T$, this gives:

$$C(\Delta y, \Delta t|y,t,y_i(t)) = \Delta y\Delta t\frac{t\dot{y}_i + y - y_i}{8\pi D_p^2 t^3}e^{-(y-y_i)^2/2D_p t}$$

Now we take the average of the correlator over the packet distribution $p(y_i,t)$ to get the expectation at a fixed y,t:

$$\langle C(\Delta y, \Delta t, |, y, t)\rangle = \int dy_i C(\Delta y, \Delta t, \left|, y, t, y_i(t)\right)p(y_i, t)$$

where $p(y_i,t) = \frac{1}{\sqrt{2\pi Tv^2 t}}e^{-y_i^2/2Tv^2 t}$ for $t \gg T$, as above. We can approximate $\dot{y}_i$ by $\langle v\rangle_{y_i,t}$ – the average velocity for a packet at position y_i as derived above. The expression for $\langle C(\Delta y,\Delta t|y,t)\rangle$ does not lend itself to a closed-form expression due to the complexity of $\langle v\rangle_{y_i,t}$; we integrate it numerically.

In nature, the strength of the turbulence will vary in space and time, so it is informative to examine how the average correlator output $\langle C(\Delta y,\Delta t|y,t)\rangle$ depends on the Lagrangian integral time scale T and the r.m.s. of the turbulent velocity field v, which controls the packet speed in the direction perpendicular to mean wind direction. We find that, for $D_p \ll D_T = v^2T$, the correlator $\langle C(\Delta y,\Delta t|y,t)\rangle$ has a clear asymmetry about $y = 0$ as expected, and that the peaks are stronger with increasing correlation time T (Extended Data Fig. 10b). Moreover, $\langle C(\Delta y,\Delta t|y,t)\rangle$ increases on average with v, while decreasing with D_p (Extended Data Fig. 10c), indicating that the response essentially derives from correlated motion over the detector rather than molecular diffusion alone.

Statistical quantification. All error bars, when shown, represent s.e.m. Statistical tests used and significance levels (P values) for given comparisons are indicated in the main text; $^*P < 5\times10^{-2}$, $^{**}P < 1\times10^{-2}$, $^{***}P < 1\times10^{-3}$, $^{****}P < 1\times10^{-4}$. In some instances, **** may refer to $P < 1\times10^{-6}$, if indicated in the text. For the plume navigation data, s.e.m. values were taken over distinct fly trajectories.

Reporting summary

Further information on research design is available in the Nature Portfolio Reporting Summary linked to this article.

Data availability

All experimental data are available at Dryad (https://doi.org/10.5061/dryad.1ns1rn8xd). Source data are provided with this paper.

Code availability

All data collection was performed using custom codes written in Python (v.3.65), using the scientific packages numpy and scipy, plotting package matplotlib and the stimulus generation package psychopy. Custom Python codes used for projecting fictive odour stimuli, for fly tracking, and for behavioural and signal extraction and smoothing are available at GitHub (https://github.com/emonetlab/opto-track).

51. Tao, L., Ozarkar, S. & Bhandawat, V. Mechanisms underlying attraction to odors in walking *Drosophila*. *PLoS Comput. Biol.* **16**, e1007718 (2020).
52. de Bruyne, M., Foster, K. & Carlson, J. R. Odor coding in the *Drosophila* antenna. *Neuron* **30**, 537–552 (2001).
53. Gorur-Shandilya, S., Martelli, C., Demir, M. & Emonet, T. Controlling and measuring dynamic odorant stimuli in the laboratory. *J. Exp. Biol.* **222**, jeb207787 (2019).
54. Pope, S. B. Simple models of turbulent flows. *Phys. Fluids* **23**, 011301 (2011).
55. Badwan, B. A., Creamer, M. S., Zavatone-Veth, J. A. & Clark, D. A. Dynamic nonlinearities enable direction opponency in *Drosophila* elementary motion detectors. *Nat. Neurosci.* **22**, 1318–1326 (2019).
56. Goldstein, S. On diffusion by discontinuous movements, and on the telegraph equation. *Q. J. Mech. Appl. Math.* **4**, 129–156 (1951).
57. Balkovsky, E. & Shraiman, B. I. Olfactory search at high Reynolds number. *Proc. Natl Acad. Sci. USA* **99**, 12589–12593 (2002).
58. Miller, C. J. & Carlson, J. R. Regulation of odor receptor genes in trichoid sensilla of the *Drosophila* antenna. *Genetics* **186**, 79–95 (2010).

Acknowledgements We thank O. Mano for help with projector troubleshooting, and A. Sehdev, E. Brown and G. Santana for help with behavioural experiments, fly rearing and discussions; V. Jayaram, J. Carlson, J. Jeanne, and the members of the Emonet laboratory for discussions and advice on the project; members of the laboratories of M. Murthy and J. Carlson for fly strains. N.K. was supported by a postdoctoral fellowship through the Swartz Foundation for Theoretical Neuroscience, by postdoctoral fellowships NIH F32MH118700 and NIH K99DC019397. M.D. was partially supported by the Program in Physics, Engineering and Biology at Yale University. B.T.M. and M.A.R. were supported by National Science Foundation grant IIS-1631864. B.D.D. was supported by an NSF GRF. D.A.C. and this research were supported by NIH R01EY026555. T.E. and this research were supported by T.E.'s setup funds from Yale University. Portions of this research were conceived at the Kavli Institute for Theoretical Physics summer school (NSF PHY-1748958).

Author contributions N.K., D.A.C. and T.E. designed the research. B.D.D. conceived the projector-based virtual set-up. N.K. and M.D. built the assay with inputs from D.A.C. and T.E.; N.K. performed all experiments, data analysis and agent-based simulations. M.D. performed the electrophysiology. B.T.M. and M.A.R. performed the numerical simulations for Fig. 5. N.K. and T.E. performed the theoretical analysis of the turbulent plume. N.K., D.A.C. and T.E. validated the data. N.K., D.A.C. and T.E. discussed the data analysis. N.K. wrote the initial draft, and N.K., D.A.C. and T.E. contributed to all revisions. All of the authors approved the final manuscript.

Competing interests The authors declare no competing interests.

Additional information
Supplementary information The online version contains supplementary material available at https://doi.org/10.1038/s41586-022-05423-4.

Correspondence and requests for materials should be addressed to Damon A. Clark or Thierry Emonet.

Peer review information *Nature* thanks Bing Brunton and the other, anonymous, reviewer(s) for their contribution to the peer review of this work. Peer reviewer reports are available.

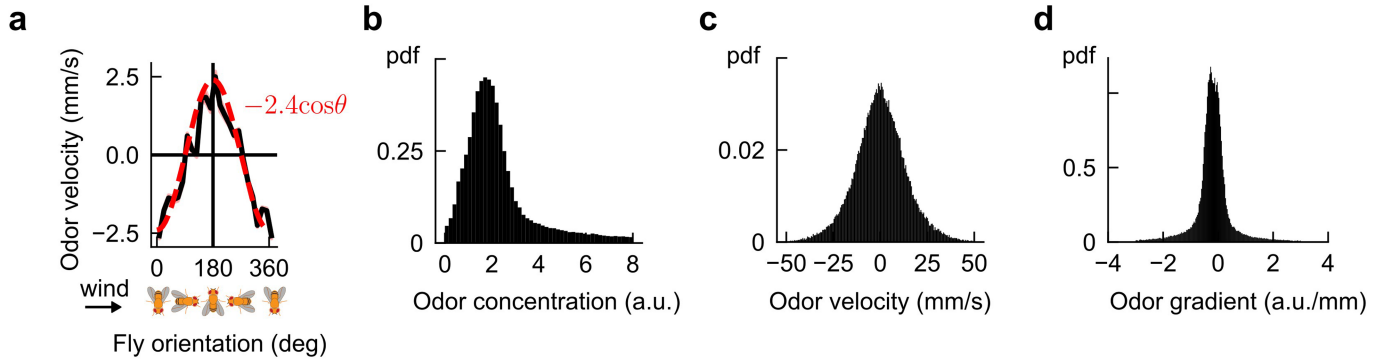

Extended Data Fig. 1 | Verification of odour velocity calculation and distributions of signal-derived quantities in measured plume. a, Mean odour velocity measured in the virtual antenna at all times for navigating flies in measured smoke plume, plotted as a function of fly orientation. The -cos(θ) trend reflects the fact that the main component of odour velocity is parallel to the mean wind direction 90^o, as expected – a consistency check on the odour velocity calculation. **b**–**d**, Histograms of signal-derived quantities measured in the fly virtual antenna; the *x*-axis limits in Fig. 1c–e are determined by the extent of these histograms.

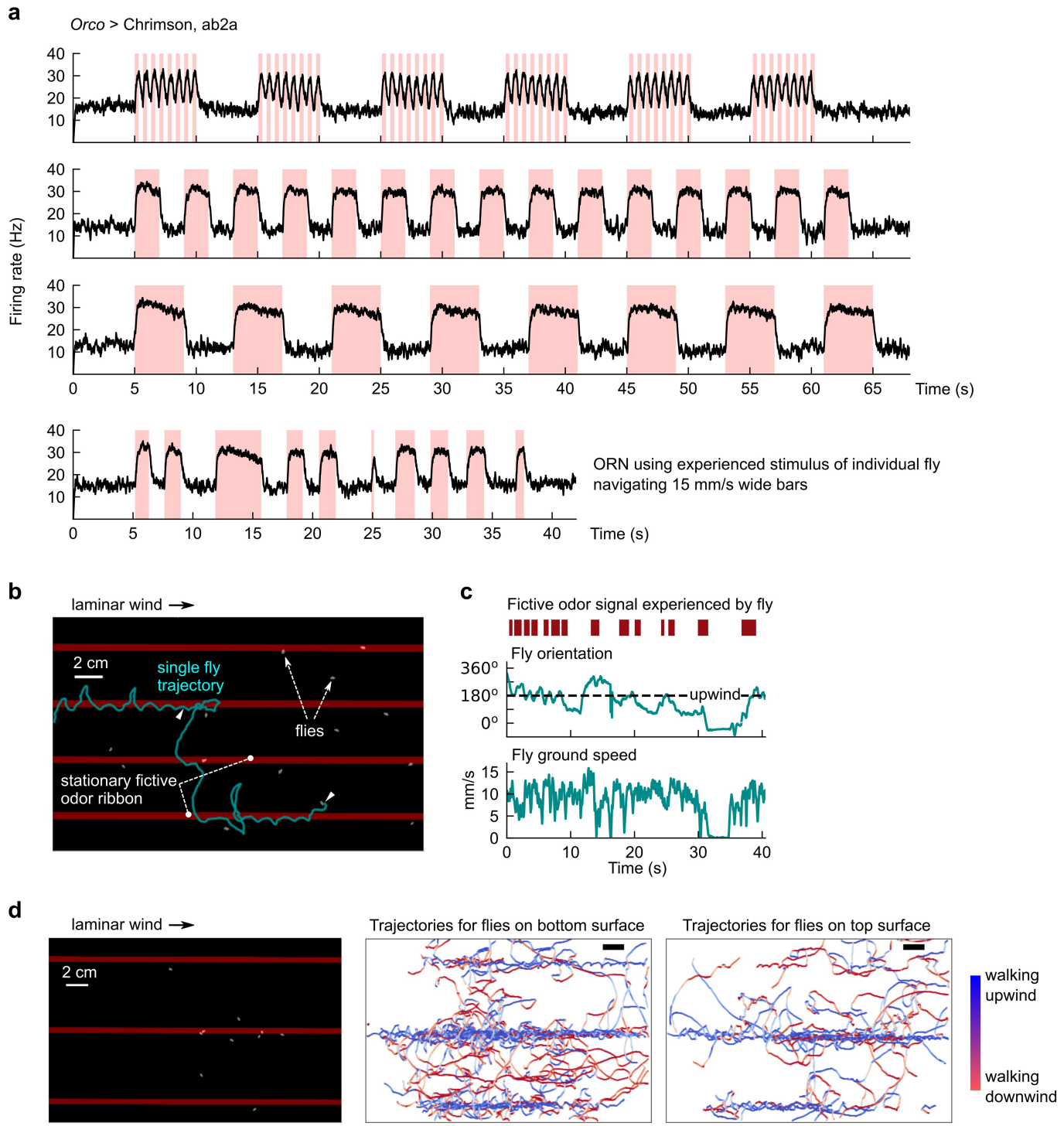

Extended Data Fig. 2 | Electrophysiological and behavioural verification of optogenetic activation of *Drosophila* ORNs. a, Extracellular measurements of ab2A firing rates for various odour signals mimicking those we use throughout our study. Stimuli (red shades) are delivered using a Luxeon Rebel 627 nm red LED (Lumileds Holding B.V., Amsterdam, Netherlands) at 10 uW/mm^2. The frequency and duty cycle for the stimuli in the first plot are 1.5 Hz and 50% respectively, which mimics what a stationary fly in the 5 cm wide, 15 mm s^{-1} fast moving bars (Fig. 2b) would encounter. Longer stimuli approximate the stimuli experienced in the wide moving bars (Fig. 2e, f). The bottom plot shows the firing rate in response to the stimulus experienced by one representative measured fly navigating 15 mm s^{-1} moving wide bars. All recordings were taken from 5 ab2a ORNs in 2 different flies. **b**, Illustrative track of a fly following stationary fictive odour ribbons upwind. Red bars: optogenetic stimulus location – bars are overlaid on the figure, but not actually imaged since the image is IR-pass filtered. **c**, Fictive odour signal experienced by a fly (red bars) can be quantified simultaneously with fly behaviour (teal) by aligning the camera and projector coordinate systems (Methods). Plotted are the fictive odour signal and behaviour for the track shown in **b. d**, Verification that flies on both the top and bottom glass surfaces of the assay respond similarly to the fictive odour signals (here, 3 odour ribbons in laminar wind; scale bar: 2 cm; left). Flies were manually annotated as being on the top or bottom surface. In both cases (middle and right; scale bar: 2 cm), flies followed the fictive odour ribbons upwind, similar to behavioural responses with real odours[10].

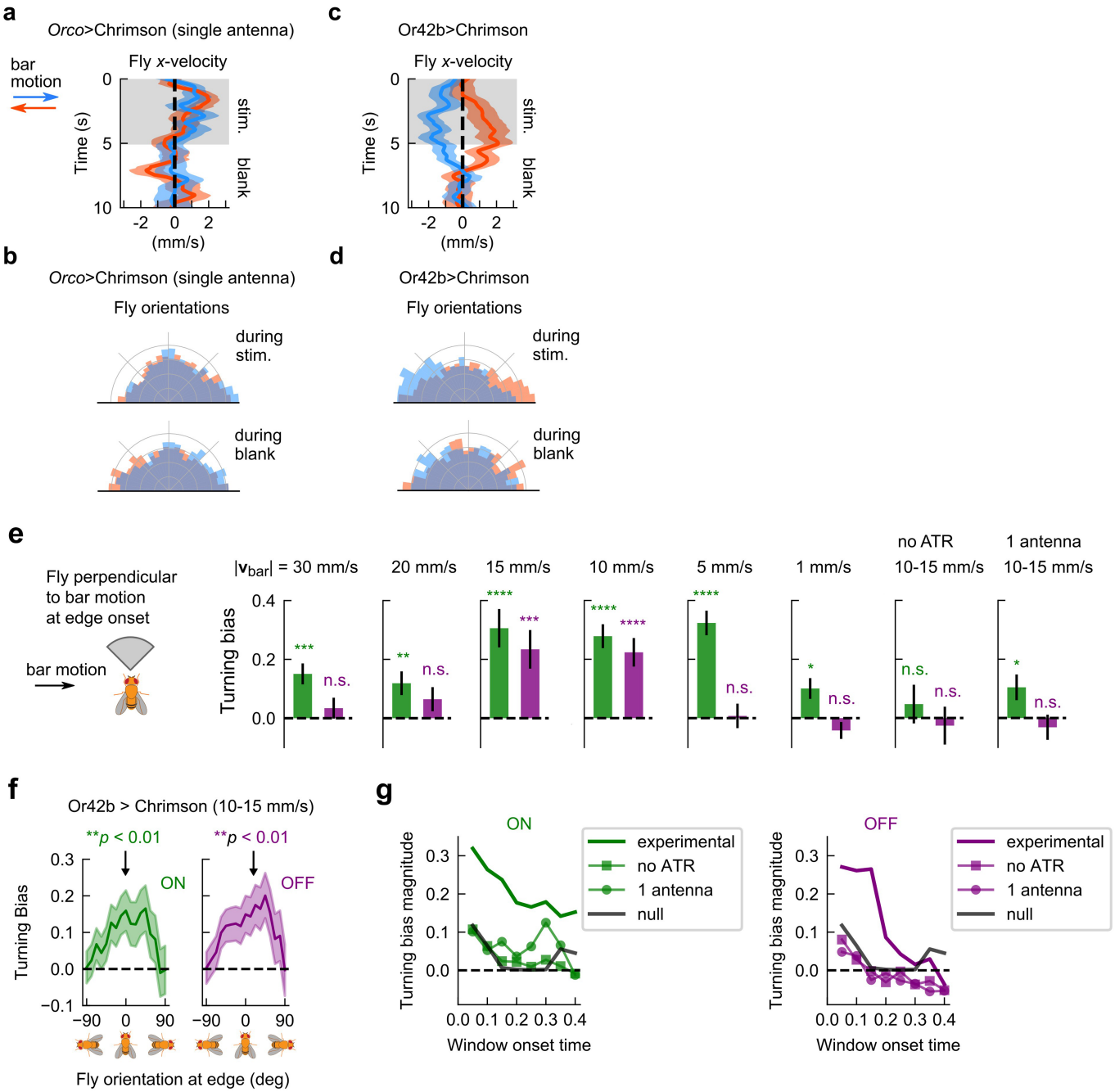

Extended Data Fig. 3 | See next page for caption.

Extended Data Fig. 3 | Odour direction selectivity in single antenna and single Or flies, and ON/OFF edge responses across speeds and for negative controls. a, Component of fly walking velocity along +*x* direction during the 5s stimulus (shaded grey) and blank periods (illustrated in Fig. 2b), in *Orco*>Chrimson flies that have one antenna ablated (compare to Fig. 2c). Shaded errors: SEM. Blue and orange denote rightward and leftward moving bars, respectively. Since it is difficult to distinguish flies walking on the top and bottom surface of the assay, right- and left-antenna ablated flies are pooled. $n = 100, 89$ tracks for rightward and leftward bar motion, respectively. Only flies oriented in the 90° sector perpendicular to the bar motion are included. **b**, Distribution of fly orientations during the 5s stimulus (top) and 5s blank periods (bottom), for rightward (blue) and leftward (orange) bar motion, *Orco*>Chrimson flies with one antenna ablated (compare Fig. 2d). Orientations are symmetrized over the *x*-axis. **c**-**d**, Same as **a**-**b**, for *Or42b*>Chrimson flies with both antennae intact. $n = 37, 50$ tracks for rightward and leftward bar motion, respectively. **e**, Turning bias for all instances in which flies encounter the fictive odour ON (green) or OFF (purple) edge, for flies oriented within a 90° sector of the direction perpendicular to bar motion. Turning bias is calculated as the sign of fly orientation change from 150 ms to 300 ms after the edge hit. All flies are *Orco*>Chrimson and fed ATR (i.e. optogenetically active) except in the 7th plot, which are not fed ATR. Data are shown for bars that move at various speeds (left 6 plots), as well as for negative controls (7th and 8th plot). Error bars: SEM. *P* values calculated using the chi-squared test (****$p < 10^{-4}$, ***$p < 10^{-3}$, **$p < 10^{-2}$, *$p < 0.05$). Specifically, $p = 9.60\times10^{-5}$ for $n = 1472$ ON edge hits and $p = 0.23$ for $n = 1661$ OFF edge hits for 30 mm s^{-1} bars; $p = 3.49\times10^{-3}$ for $n = 1167$ ON edge hits and p = 0.132 for $n = 1306$ OFF edge hits for 20 mm s^{-1}; $p = 1.03\times10^{-6}$ for $n = 548$ ON edge hits and $p = 1.18\times10^{-3}$ for $n = 470$ OFF edge hits for 15 mm s^{-1}; $p<10^{-6}$ for $n = 1125$ ON edge hits and $p = 1.78\times10^{-5}$ for $n = 1039$ OFF edge hits for 10 mm s^{-1}; $p < 10^{-6}$ for $n = 1000$ ON edge hits and p = 0.816 for N=987 OFF edge hits for 5 mm s^{-1}; $p = 0.012$ for $n = 1284$ ON edge hits and p = 0.2106 for $n = 1633$ edge hits for 1 mm s^{-1}; $p = 0.423$ for $n = 1387$ ON edge hits and $p = 0.701$ for $n = 1484$ OFF edge hits for no ATR 10-15 mm s^{-1}; and $p = 0.0295$ for $n = 988$ ON edge hits and $p = 0.454$ for $n = 1153$ OFF edge hits for 1 antenna 10-15 mm s^{-1}. Direction selectivity is satisfied if both ON and OFF edge responses have the same sign; gradient sensing would require opposite signs for the two edges. Data indicate that flies counterturn against the direction of fictive odour bars at both edges, within a range of bar speeds. Large ON responses for slow bar speeds are likely attributed to gradient sensing: since the direction of odour motion and gradients are the same for ON edges but opposite for OFF edges, this would give appreciable ON edge responses at slower speeds, but diminished OFF edge responses. **f**, Turning responses for Or42b > Chrimson flies, in which light activates only one ORN type, in response to bars moving at 10-15 mm s^{-1}. Error shades: SEM. Turning responses are consistent with direction selectivity (compare with Fig. 2f). $p = 4.82\times10^{-3}$ for $n = 706$ ON edge hits and $p = 5.51\times10^{-3}$ for $n = 763$ OFF edge hits. **g**, Dependence of the results on the choice of the window over which the turning bias is calculated. The *x*-axis shows the onset time of the window; the offset time was 150 ms later. The *y*-axis plots the turning bias for flies oriented within a 90° sector of the direction perpendicular to bar motion (as in **e**). "Experimental" flies refer to *Orco* > Chrimson in response to bars moving at 10–15 mm s^{-1} (same as in Fig. 2); "no-ATR" and "1 antenna" are the same flies not fed ATR or with only 1 antenna, respectively. The "null" condition is calculated using random chosen trajectories and calculating angle changes following fictitious moving bars at random angles not actually presented to the flies. Over window onsets of 0-200 ms, the *no ATR*, *1 antenna* and *null* responses are all within the same regime (< ~0.1), while the experimental responses are significantly higher. These results are consistent with previous findings. OFF response reaction times of ~500 ms have been observed[9], but those were for flies counterturning back into static ribbons – the differing locomotive repertoire (flying vs. walking) and plume dynamics (static vs. dynamic) would account for this discrepancy. Reaction times of 400 ms have been observed for walking flies, but this may reflect imprecision in odour delivery[6]; indeed, reaction times are as low as 100 ms for tethered flies whose ORNs are stimulated optogenetically[17] and as low as 85ms when ORNs are stimulated with real odours[25].

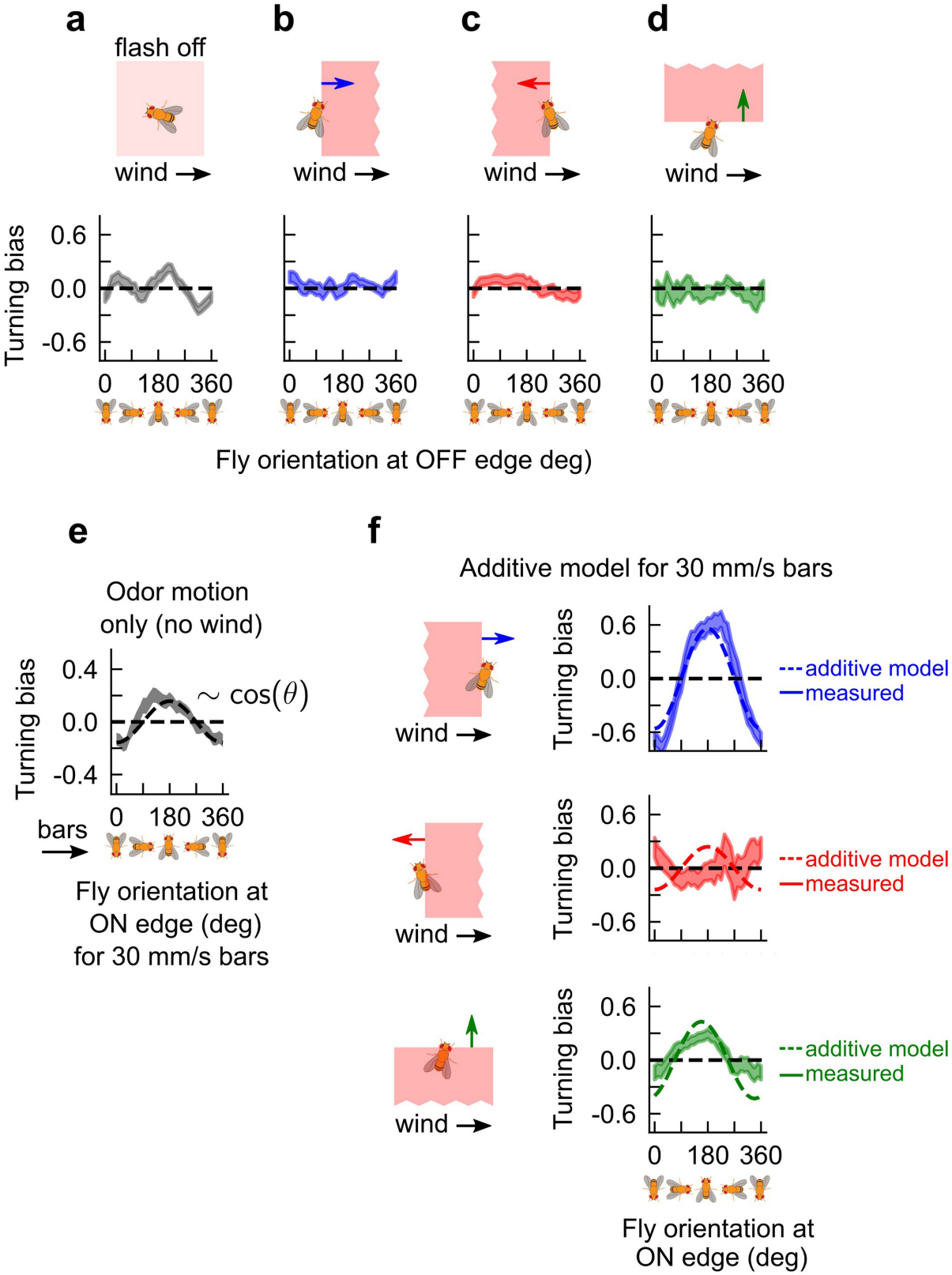

Extended Data Fig. 4 | OFF edge responses in laminar wind and ON edge responses for fast 30 mm s^{-1} bars. a, Turning bias versus fly orientation when bilateral optogenetic stimulus is turned off (compare with the first plot in Fig. 3b for flash onset). $n = 1490$ OFF flash hits. **b**–**d**, Fly turning bias for 15 mm s^{-1} bars moving parallel, antiparallel, and perpendicular to 150 mm s^{-1} laminar wind (compare with Figs. 3de). Shaded errors: SEM. $n = 1493$, 1588, and 671 OFF edge encounters for bars parallel, antiparallel, and perpendicular to the wind, respectively. **e**, Fly turning bias vs. fly orientation at ON edge for faster 30 mm s^{-1} fictive odour bars without wind (analogous to 15 mm s^{-1} bar responses in second plot of Fig. 3c). Dotted line: fit of response to $-0.16\cos\theta$. $N = 1472$ ON edge encounters. **f**, Additive model for ON edges of 30 mm s^{-1} bars; analogous to Figs. 3de. Solid shaded region: mean ± 1 SEM; dotted lines: additive model prediction. $N = 323$, 319, and 1013 ON edge encounters for odour bars with parallel, antiparallel, and perpendicular to the wind, respectively.

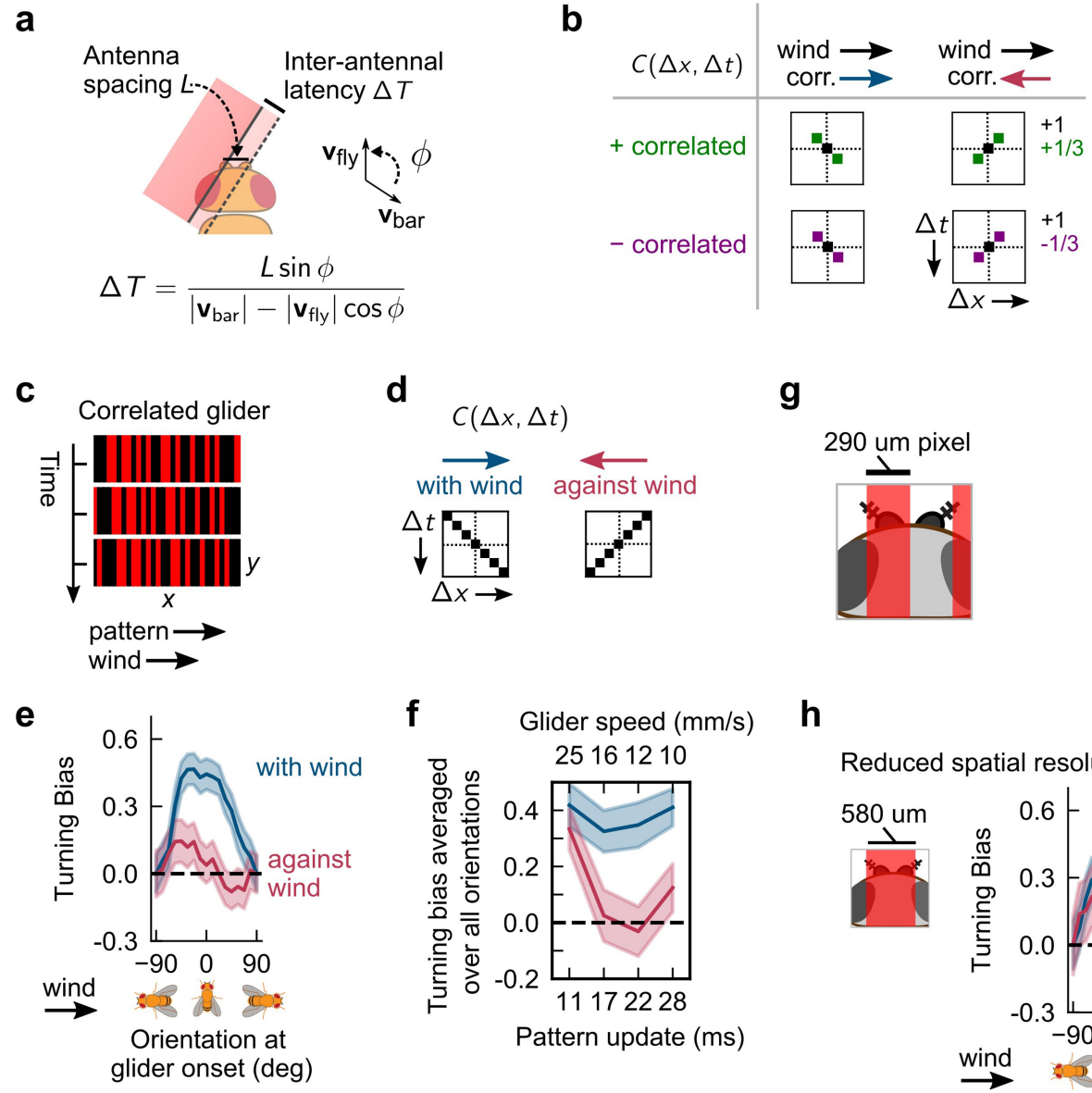

Extended Data Fig. 5 | See next page for caption.

Extended Data Fig. 5 | Supplementary figures and additional evidence that direction sensing is enacted using a correlation-based algorithm. **a**, Schematic illustrating calculation of latency ΔT between antennae hits for moving edges. Correlation-based models for direction selectivity depend on the latency ΔT of the time at which the edge hits the two sensors – in this case, the fly's two antennae. Measuring ΔT does not require resolving the image or stimulus at antennal resolution (~300 μm), rather ΔT can be inferred with knowledge of the fly's orientation relative to the bar direction ϕ, as well as the speeds of the fly and bar – all of which are known. See Methods for details of the calculation and an estimate of the uncertainty. **b**, Spatiotemporal correlation functions for correlated noise stimuli (Fig. 4c–f). Each type of correlated noise stimulus is characterized by the correlation function $C(\Delta x, \Delta t)$ computed between all pairs of bars separated spatiotemporally by Δx pixels and Δt frames. Since our stimuli are generated by summing and binarizing Gaussian variables, nonzero correlations off of the origin have magnitude 1/3[26]. For example, for positively correlated with-wind stimuli (top left plot), $C(1, 1) = C(-1, -1) = 1/3$, and the remaining correlations are zero, while for negatively correlated with-wind stimuli (bottom left plot), $C(1, 1) = C(-1, -1) = -1/3$. **c**, Snapshots of *glider* stimulus with correlations along $+x$ axis, for 3 consecutive frames. In one instance of time, the stimulus is a random pattern of light and dark 1-pixel-wide bars perpendicular to the 150 mm s^{-1} laminar wind. Each x-pixel is perfectly correlated with the pixel to its right in the next frame; thus the pattern in the next frame is the same as the pattern in the current frame, but shifted by one pixel. Visually, this would be perceived as a fixed pattern moving coherently to the right in discrete steps. **d**, Like correlated noise stimuli, gliders are defined by their correlation matrix $C(\Delta x, \Delta t)$. Unlike correlated noise, the correlations i) have magnitude 1, and ii) exist for many spacetime points. That is, for rightward correlated gliders, a given pixel in a given frame is perfectly correlated with the pixel to its right one frame later, but also with the second pixel to its right 2 frames later, etc. Thus $C(\Delta x, \Delta t)$ has values +1 along the diagonal. Similarly, $C(-\Delta x, \Delta t)$ has values 1 along the anti-diagonal. Since $+x$ points downwind, we call gliders with correlations to the right "with-wind", and gliders with correlations to the left "against-wind," in analogy to the correlated noise stimuli (Fig. 4d). **e**, Turning bias versus fly orientation for with-wind (blue) and against-wind (red) gliders. Data using pattern update rates of 45 or 60 Hz are pooled. Shaded errors: SEM. Gliders are presented in 4s blocks, interleaved with 4s of no stimulus. Turning bias is defined as the sign of the change in orientation from 200 to 500 ms after the block onset. We only used flies with speeds < 12 mm s^{-1} for gliders, since long-range correlations can interfere with the intended correlation if fly walking speed is near the glider speed. $n = 301$, 247 onset events, for with-wind and against-wind, respectively. **f**, Turning bias averaged over all orientations for different glider speeds. Glider speed is calculated as (pixel width)×(pattern update rate) where the pixel width is 290 µm and the pattern rate is some multiple of the inverse frame rate, 1/(180 Hz). $n = 141, 163, 138, 190$ onset events for with-wind stimuli at glider speeds 25, 16, 12, and 10 mm s^{-1}, respectively; $n = 159, 119, 128, 137$ onset events for against-wind stimuli at same glider speeds, respectively. **g**, For correlated stimuli to be sensed in our assay, the bar width (size of x-pixel, 290 µm), must be on the order of the fly antennal separation (~300 µm[58]). **h**, Glider stimuli experiments repeated for bars that were double the width, 580 µm. Differences now disappear for with and against-wind correlations, consistent with bilaterally enabled direction sensing, since these bars are too wide to consistently stimulate antennae differentially. Shaded errors: SEM. $n = 195, 169$ onset events for with-wind and against-wind, respectively.

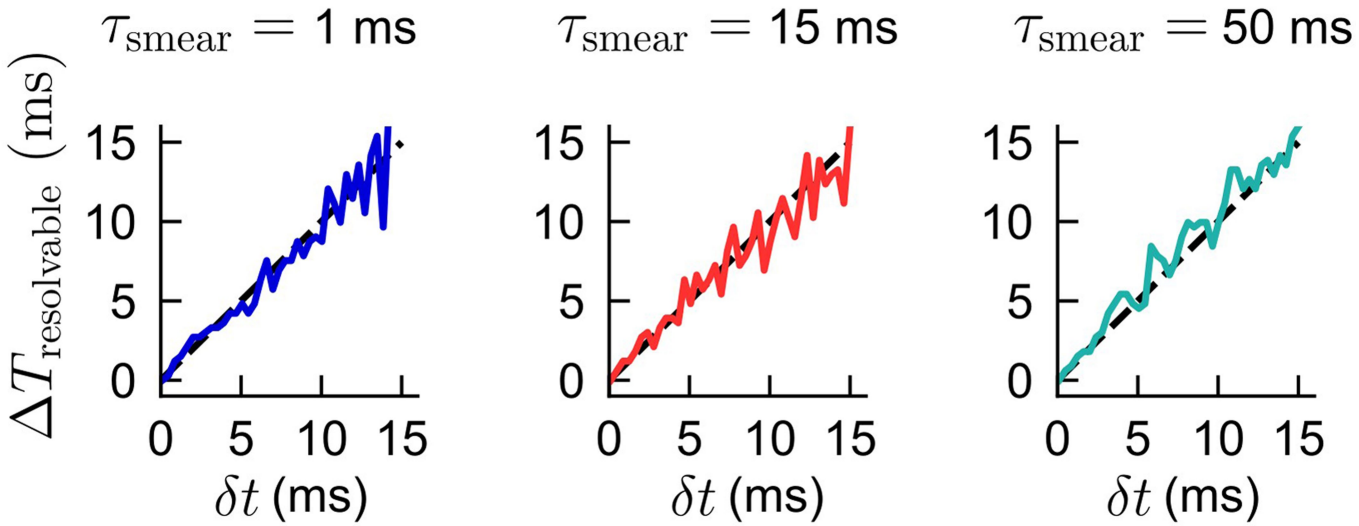

Extended Data Fig. 6 | HRC response is robust to signal pre-filtering. Minimum resolvable inter-antennal latency ΔT as a function of the noise level, for exponential pre-filters of varying timescale, $\tau_{\mathrm{smear}} = 1, 15, 50$ ms, respectively, for the 3 plots. Noise level is quantified as a random shift of ΔT, where each shift is chosen from a normal distribution with mean zero and standard deviation δt. The HRC's delayed arm has an exponential filter of timescale $\tau_{\mathrm{HRC}} = 15$ ms. Dotted line: identity. A particular value of ΔT is deemed resolvable if the SD over HRC responses is greater than the mean over HRC responses (see Methods for details). The mean and SD are calculated over 100 samples (i.e. 100 random shifts of ΔT) for a given noise level δt.

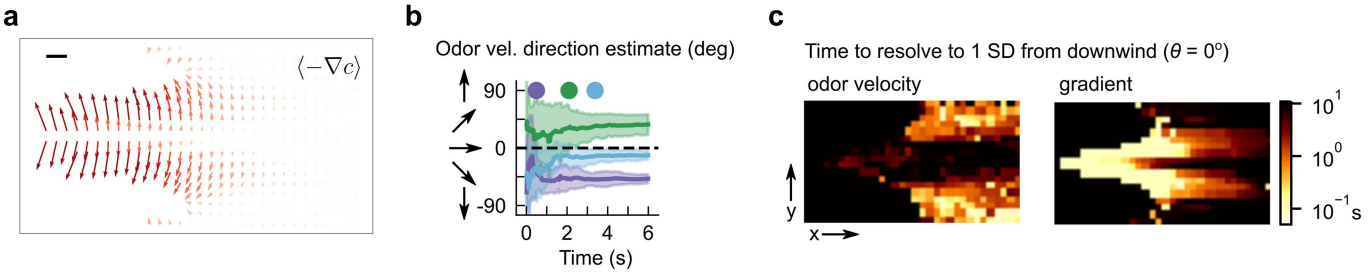

Extended Data Fig. 7 | Odour velocity and concentration gradients provide complementary directional information in complex plumes. a, Vector field of the negative gradient of odour concentration $-\nabla c$, averaged over the full simulation (compare to Fig. 6c in the main text). Gradients contain strong lateral components near the odour source. **b**, Time course of an estimate of the direction of odour motion $\theta_{\text{odor}} = \tan^{-1}\left(\mathbf{v}_{y,\text{odor}}, \mathbf{v}_{x,\text{odor}}\right)$ at the centre of the boxed regions in Fig. 6a, determined by averaging all detectable θ in the past t seconds. Error bars are found by repeating this for 16 different 10 s time windows throughout the simulation, and taking the average and standard deviation over these 16 samples – these correspond to the mean and standard error of the mean. Dots indicate the time needed to distinguish the direction of odour motion from 0° (downwind) with a 68% confidence level for the 3 regions. **c**, Heatmap of time taken to distinguish the direction of odour motion from 0° to within 68% confidence for fixed locations throughout plume. Black values include the possibility that the odour motion direction is not distinguishable from downwind no matter how long one samples.

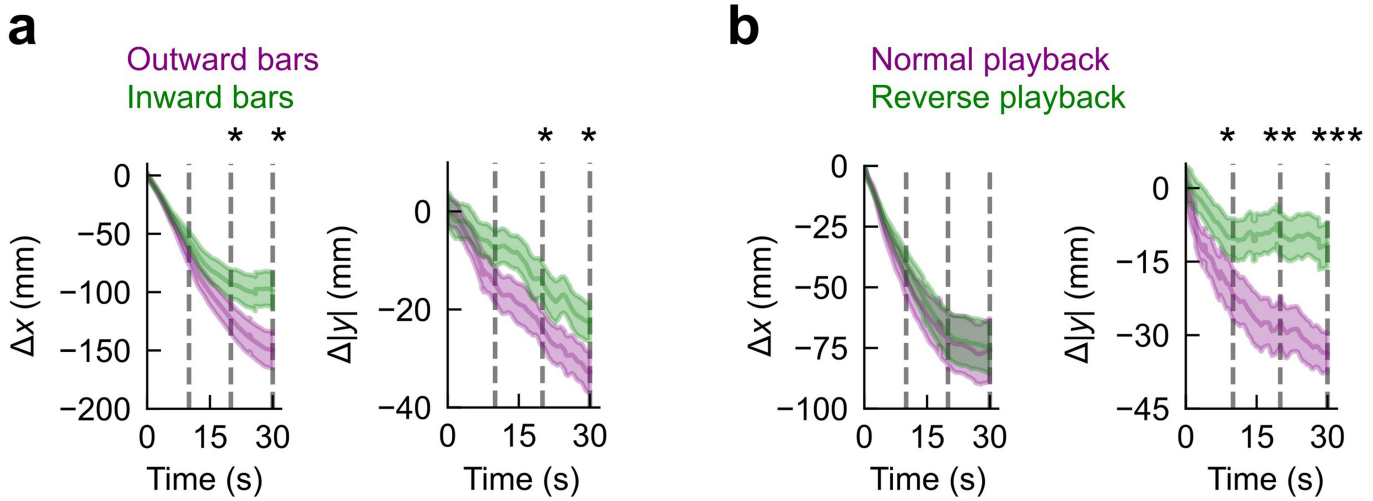

Extended Data Fig. 8 | Odour motion sensing aids plume navigation by increasing lateral motion toward the plume centerline. a, Average change in position parallel to wind, x (left), and away from the plume centerline, $|y|$ (right), in outward (purple) and inward (green) moving bars plume (Fig. 6d), as a function of time. Note that $x = 0$, $y = 0$ is the fictive plume's odour source location. The initial values at $t = 0$ of x (y) were subtracted, so the change Δx (Δy) is plotted – this is negative because flies progress toward to the centerline (decreasing y) and upwind (decreasing x). Only flies beginning in the rear 50 mm of the arena and which navigated for at least 30s were considered. Shades: SEM over distinct fly trajectories. Dotted lines: times $t = 10, 20, 30$s. By $t = 20$s, flies in the outward bar plume have made more progress both in the upwind direction ($p = 0.025$; 1-tailed t-test) and toward the plume centerline ($p = 0.032$; 1-tailed t-test). **b**, same for fictive odour plume shown in Fig. 6g, played normally (purple) or in reverse (green). Here, flies make equal progress upwind by 30s (left plot), but significantly faster progress toward the plume centerline in the forward played plume than the reverse one (right plot) ($p = 0.035$ at $t = 10$s, $p = 3.0\times10^{-3}$ at $t = 20$s, at $p = 1.6\times10^{-4}$ at $t = 30$s; 1-tailed t-test). Shades: SEM over distinct fly trajectories.

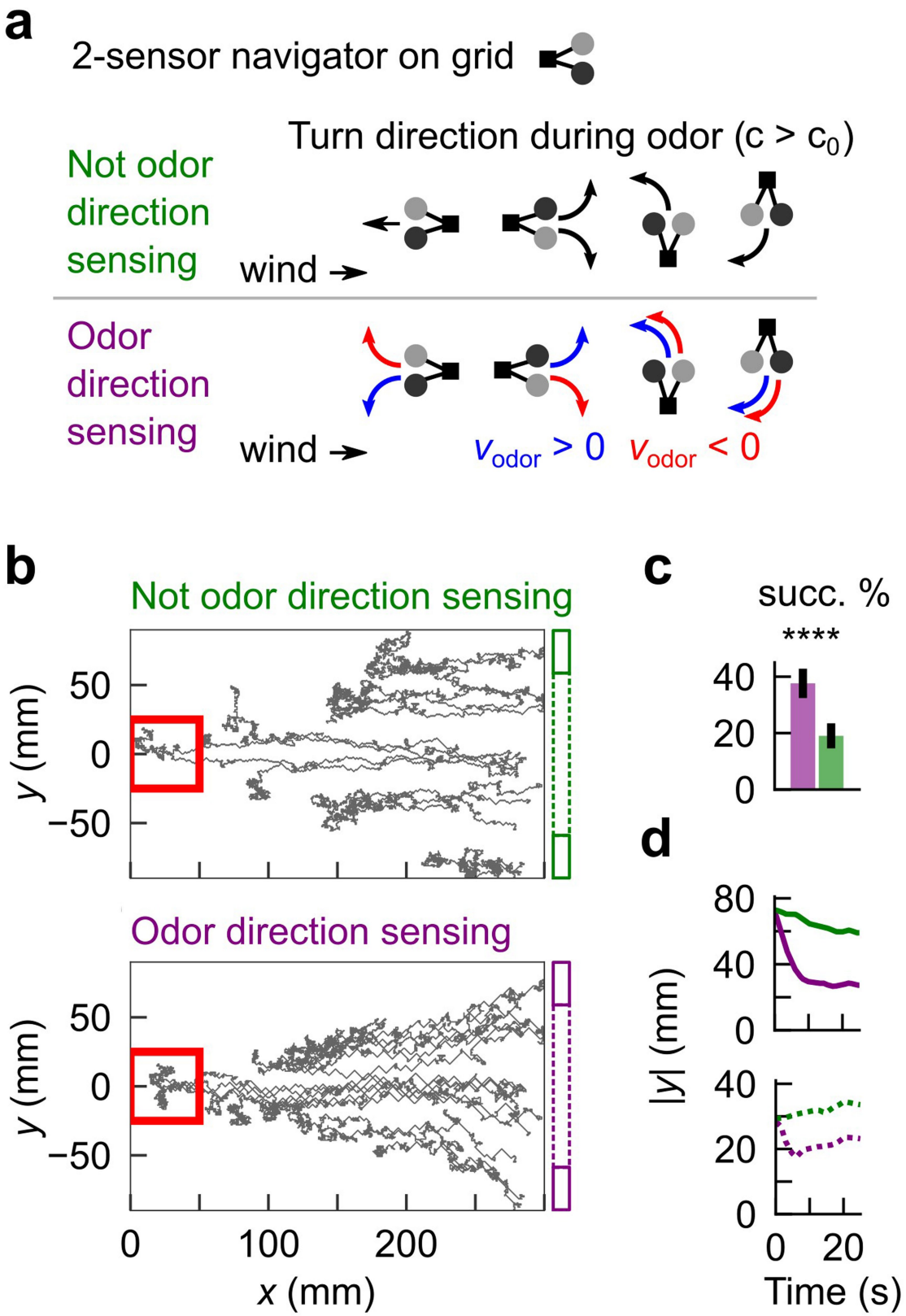

Extended Data Fig. 9 | See next page for caption.

Extended Data Fig. 9 | Odour motion sensing enhances performance of virtual robots obeying a simple navigation strategy on a grid. a, Model of 2-sensor virtual agents navigating the simulated odour plume (Fig. 6a). Agents are always oriented at 0°, 90°, 180° or 270°, and at each timestep turn 90° either left or right and move forward one step. Agents are either odour direction sensing (DS+) or not odour direction sensing (DS-). When odour concentration c exceeds some threshold c_0, DS- agents turn upwind. DS+ agents, for $c > c_0$, turn against the direction of odour motion when oriented upwind or downwind; crosswind agents always turn upwind. DS+ agents infer the direction of odour signals using an HRC-like computation between their 2 sensors (Methods). **b**, Example trajectories of robots navigating plume in **a**, when they are initialized in the back 50 mm of the arena, for DS- (top) and DS+ (bottom) agents. **c**, Percentage of 500 agents reaching the 50x50 mm red source region; more DS+ agents reach the source than DS- agents (38% vs. 19%; $p < 10^{-6}$; 1-tailed t-test) **d**, Lateral distance from plume axis $|y|$ over time, for agents initialized near the plume edges (>60 mm from plume axis, indicated by the solid boxes in **b**; top plot) or near the plume axis (<60 mm from axis, indicated by the dashed boxes in **b**; bottom plot). Odour direction sensing enhances lateral drift toward the plume centerline, particularly for robots initialized at the plume edges.

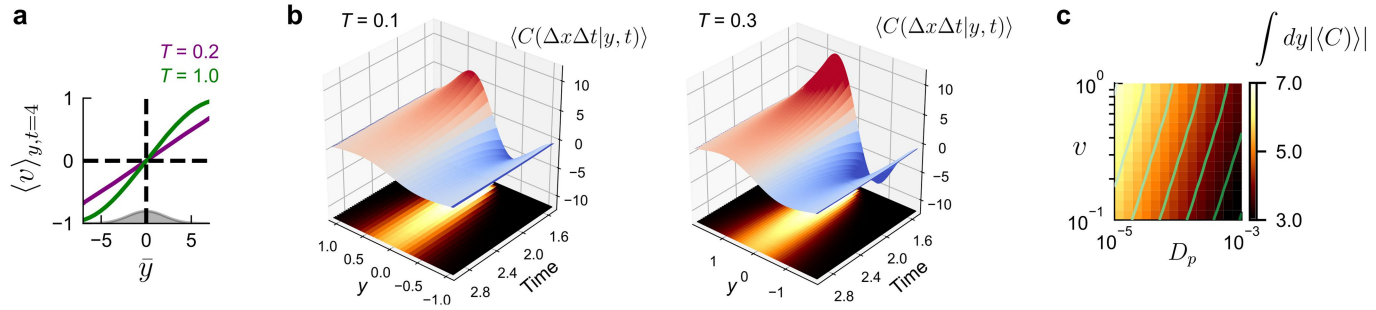

Extended Data Fig. 10 | Odour velocity in model of turbulent plumes points outward from plume centerline and is computed by local space-time correlators. We use a simple packet model of turbulent plumes. Packets are released from a source and disperse in the lateral direction while being advected downwind (see Methods for model and calculation details). **a**, Packet velocity $\langle v \rangle_{y,t}$ in the plume model, as a function of $\bar{y} = y/\sqrt{T}$, for two correlation times, $T = 0.2$ (purple) and $T = 1$ (green), at a fixed time $t = 4$. Here, v is set to 1. To directly compare velocity for plumes with different T, (and therefore different diffusivities) we plot the velocity versus the normalized length $\bar{y}$. Specifically, since $\langle y^2 \rangle = 2Tv^2t$ for $t \gg T$ then at a given t, the packet distribution in terms of $\bar{y}$ is the same for plumes with distinct T. The distribution of packets for either T is a function of $\bar{y}$ shown in grey. The velocity is an odd function of y, i.e. it points outward from the plume axis. In addition, the asymmetry is steeper for higher correlation times. **b**, The value of the correlator $\langle C(\Delta y, \Delta t|y, t)\rangle$ as a function of lateral distance y, for various times t for $T = 0.1$ (left) and $T = 0.3$ (right). Here, $D_p = 0.005$. Since the packets are advected downwind with a velocity $U \gg v$, the time axis is proportional to the downwind distance. The packet distribution is shown on the bottom; the limits of the y-axis are chosen such that the plume extents are the same in both plots. **c**, The total y-integral of the absolute value of $\langle C(\Delta y, \Delta t|y, t)\rangle$ at a fixed $t = 4$, as a function of odour packet speed (y-axis) and molecular diffusivity (D_p), with $T = 1$, $v = 1$. This integral indicates the degree of directional sensing on average. The integral is highest for greater packet speeds and lower molecular diffusivities (top left corner).

nature portfolio

Corresponding author(s): Emonet, Thierry
Clark, Damon

Last updated by author(s): Jun 2, 2022

Reporting Summary

Nature Portfolio wishes to improve the reproducibility of the work that we publish. This form provides structure for consistency and transparency in reporting. For further information on Nature Portfolio policies, see our Editorial Policies and the Editorial Policy Checklist.

Statistics

For all statistical analyses, confirm that the following items are present in the figure legend, table legend, main text, or Methods section.

n/a	Confirmed
☐	☒ The exact sample size (*n*) for each experimental group/condition, given as a discrete number and unit of measurement
☐	☒ A statement on whether measurements were taken from distinct samples or whether the same sample was measured repeatedly
☐	☒ The statistical test(s) used AND whether they are one- or two-sided *Only common tests should be described solely by name; describe more complex techniques in the Methods section.*
☐	☒ A description of all covariates tested
☐	☒ A description of any assumptions or corrections, such as tests of normality and adjustment for multiple comparisons
☐	☒ A full description of the statistical parameters including central tendency (e.g. means) or other basic estimates (e.g. regression coefficient) AND variation (e.g. standard deviation) or associated estimates of uncertainty (e.g. confidence intervals)
☐	☒ For null hypothesis testing, the test statistic (e.g. *F*, *t*, *r*) with confidence intervals, effect sizes, degrees of freedom and *P* value noted *Give P values as exact values whenever suitable.*
☒	☐ For Bayesian analysis, information on the choice of priors and Markov chain Monte Carlo settings
☒	☐ For hierarchical and complex designs, identification of the appropriate level for tests and full reporting of outcomes
☒	☐ Estimates of effect sizes (e.g. Cohen's *d*, Pearson's *r*), indicating how they were calculated

Our web collection on statistics for biologists contains articles on many of the points above.

Software and code

Policy information about availability of computer code

Data collection	All data collection was performed using custom codes written in Python (version 3.7), along with the PsychoPy package (version 2020.2.4.post1). Codes for projecting stimuli and tracking flies are available at: https://github.com/emonetlab/opto-track
Data analysis	All data collection was performed using custom codes written in Python (version 3.7). The following packages (and their versions) were used in Python: numpy (1.16.4), scipy (1.3.1), and matplotlib (3.1.0). All data were analyzed with custom written scripts. Code related to processing fly and stimuli data are at: https://github.com/emonetlab/opto-track

For manuscripts utilizing custom algorithms or software that are central to the research but not yet described in published literature, software must be made available to editors and reviewers. We strongly encourage code deposition in a community repository (e.g. GitHub). See the Nature Portfolio guidelines for submitting code & software for further information.

Data

Policy information about availability of data

All manuscripts must include a data availability statement. This statement should provide the following information, where applicable:

- Accession codes, unique identifiers, or web links for publicly available datasets
- A description of any restrictions on data availability
- For clinical datasets or third party data, please ensure that the statement adheres to our policy

All data are deposited in Dryad (https://doi.org/10.5061/dryad.1ns1rn8xd.).

Human research participants

Policy information about studies involving human research participants and Sex and Gender in Research.

Reporting on sex and gender	not applicable
Population characteristics	not applicable
Recruitment	not applicable
Ethics oversight	*Not applicable*

Note that full information on the approval of the study protocol must also be provided in the manuscript.

Field-specific reporting

Please select the one below that is the best fit for your research. If you are not sure, read the appropriate sections before making your selection.

☒ Life sciences ☐ Behavioural & social sciences ☐ Ecological, evolutionary & environmental sciences

For a reference copy of the document with all sections, see nature.com/documents/nr-reporting-summary-flat.pdf

Life sciences study design

All studies must disclose on these points even when the disclosure is negative.

Sample size	No statistical tests were used to determine sample size. We used more than 50 flies per experimental condition. Flies were reared at 10-15 flies per vial, so this gave 3-5 separate vials for each experimental condition, sufficient to remove any outlier effects related to a single vial.
Data exclusions	Individual flies designated as non-behaving(average speed < 2 mm/s during experiment) were excluded from all analysis, as these were nonbehaving flies. For natural plume experiments, (Fig. 6), only tracks lasting longer than 30 s were included in the analyses, so that individual fly identity could be tracked.
Replication	All experiments were replicated more than three times on the same flies and the same conditions were replicated at least 10 times with different flies over several days.
Randomization	All flies in a given vial were tested on the same protocols, at the same time, in the behavioral assay; thus, they were not allocated into specific subgroups at any point once reared. All similar experiments were randomly interleaved -- e.g. the direction of moving bars was chosen randomly for each instantiation of an experiment.
Blinding	The investigators were not blind to fly genotypes. Blinding was not possible, as crosses were done by the investigator also performing the experiment.

Reporting for specific materials, systems and methods

We require information from authors about some types of materials, experimental systems and methods used in many studies. Here, indicate whether each material, system or method listed is relevant to your study. If you are not sure if a list item applies to your research, read the appropriate section before selecting a response.

Materials & experimental systems

n/a	Involved in the study
☒	☐ Antibodies
☒	☐ Eukaryotic cell lines
☒	☐ Palaeontology and archaeology
☐	☒ Animals and other organisms
☒	☐ Clinical data
☒	☐ Dual use research of concern

Methods

n/a	Involved in the study
☒	☐ ChIP-seq
☒	☐ Flow cytometry
☒	☐ MRI-based neuroimaging

Animals and other research organisms

Policy information about studies involving animals; ARRIVE guidelines recommended for reporting animal research, and Sex and Gender in Research

Laboratory animals	Drosophila melanogaster; genotypes used: w;gmr-hid;+ ;+;20XUAS-Chrimson w;+;Orco-Gal4, w;+;Or42b-Gal4 , w;gmr-hid/+;20XUAS-Chrimson/Orco-Gal4, w;gmr-hid/+;20XUAS-Chrimson/Or42b-Gal4
Wild animals	No wild animals were used in this study.
Reporting on sex	All experiments were carried out on female flies.
Field-collected samples	No field collected samples were used in this study
Ethics oversight	This study did not require ethical approval

Note that full information on the approval of the study protocol must also be provided in the manuscript.